We are IntechOpen, the world's leading publisher of Open Access books Built by scientists, for scientists

6,900
Open access books available

185,000
International authors and editors

200M
Downloads

Our authors are among the

154
Countries delivered to

TOP 1%
most cited scientists

12.2%
Contributors from top 500 universities



WEB OF SCIENCE™

Selection of our books indexed in the Book Citation Index in Web of Science™ Core Collection (BKCI)

Interested in publishing with us?
Contact book.department@intechopen.com

Numbers displayed above are based on latest data collected.
For more information visit www.intechopen.com



Chapter 7

Chip-Scale Microwave Photonic Signal Processing

Jian Wang and Yun Long

Additional information is available at the end of the chapter

http://dx.doi.org/10.5772/66322

Abstract

The use of optical technology can provide unprecedented performance to the generation, distribution, and processing of microwave. Recently, on-chip microwave photonics (MWP) has gained significant interests for its numerous advantages, such as robustness, reconfigurability as well as reduction of size, weight, cost, and power consumption. In this chapter, we review our recent progress in ultracompact microwave photonic signal processing using silicon nanophotonic devices. Using the fabricated silicon waveguide, silicon microring resonators (MRRs) and silicon photonic crystal nanocavities, we demonstrate on-chip analog signal transmission, optically controlled tunable MWP filter, and ultrahigh peak rejection notch MWP filter. The performance of analog links and the responses of MWP filters are evaluated in the experiment. In addition, microwave signal multiplication and modulation are also demonstrated based on a silicon Mach-Zehnder modulator in the experiment with favorable operation performance. The demonstrated on-chip analog links, MWP filters, microwave signal multiplication/modulation may help understand on-chip analog signaling and expand novel functionalities of MWP signal processing.

Keywords: optical signal processing, microwave photonics, analog transmission, silicon photonics, microring resonator, photonic crystal nanocavity, microwave photonic filter

1. Introduction

Silicon photonics has become one of the most promising photonic integration platforms owing to its small footprint, low power consumption, and availability of complementary metal-oxide-semiconductor (CMOS) fabrication technology for low-cost mass production [1–4]. Typical silicon nanophotonic devices include silicon waveguides, silicon microring resonators (MRRs), and silicon photonic crystal [5–10], showing unprecedented small size for potential large-scale integration [11–16]. The great success of silicon photonics benefits from the rapid growth of digital optical communications systems such as high capacity optical communications and optical interconnects [4, 17–34].

INTECH
open science | open minds

© 2017 The Author(s). Licensee InTech. This chapter is distributed under the terms of the Creative Commons Attribution License (http://creativecommons.org/licenses/by/3.0), which permits unrestricted use, distribution, and reproduction in any medium, provided the original work is properly cited. CC BY

It has been proved that photonic systems can be also applied to deliver analog signals and process microwave radio frequency (RF) signals in the optical domain, deriving an emerging subject called microwave photonics (MWP) [35, 36]. The initial of MWP was for distributing microwave signal over long distances. However, the applications have evolved dramatically and now include photonic generation of microwave signal [37–40], photonic processing of microwave signal [41–50], frequency measurement of microwave signal [51, 52], and so on. MWP signal processing is of great importance among these applications. As shown in **Figure 1**, MWP signal processing functionalities include microwave signaling [53, 54], filtering [42, 43, 47], differential [48–50], integral [55, 56], pulse shaping [57, 58], Hilbert transformation [59], arbitrary waveform generation [60–63], frequency multiplication [64, 65], beamforming [66, 67], and more.

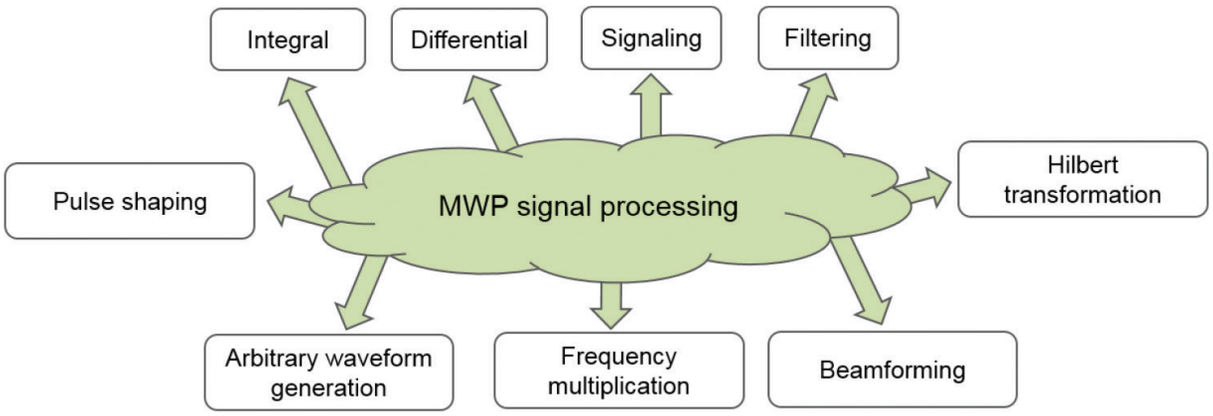


Figure 1. Functionalities classification of MWP signal processing.

Traditional MWP signal processing technologies are mainly based on fibered devices. Recently, there has been an increasing interest on developing integrated components to realize MWP signal processing functionalities. Adopting integrated photonics technologies in MWP signal processing will address the issues such as stability and compactness in traditional fiber-based devices. Very recently, owning to the advance on silicon photonics, some microwave photonic devices such as MWP filters [41, 43, 47, 68], on-chip pulse shapers [57, 58], differentiators [48–50], and Hilbert convertors [59], and ultra wide band (UWB) signal generators [69] have been implemented on silicon on insulator (SOI) platforms. **Figure 2** shows the basic schematic illustration of microwave photonic signal processing using a silicon chip. Usually, a laser source emits a continuous wave (CW) light. The RF signal is generated using a RF generator. After modulation, the RF signal carried by the light carrier is launched to a silicon chip for signal processing. After that, a photodiode is used to convert optical signal to RF signal for detection. The basic silicon photonic devices for MWP signal processing include silicon waveguide, microdisk, microring resonator (MRR), photonic crystal (PhC) nanocavity, Mach-Zehnder modulator (MZM), Bragg grating, and more, as shown in **Figure 3** [70]. Based on the combination of these elementary elements, many complicated MWP processing functionalities can be realized.

In this chapter, we review our recent works in chip-scale microwave photonic signal processing. First, we present the progress of on-chip analog signal transmission. We analyze the

performance of on-chip analog signal transmission using the fabricated silicon waveguide and resonators, that is, microring resonators and photonics crystal nanocavities. Second, we report the progress of MWP filters, various types of MWP filters are introduced, and the impact of optical nonlinearities on MWP filters is also discussed. Finally, we show the results of on-chip photonic-assisted microwave signal multiplication and modulation.

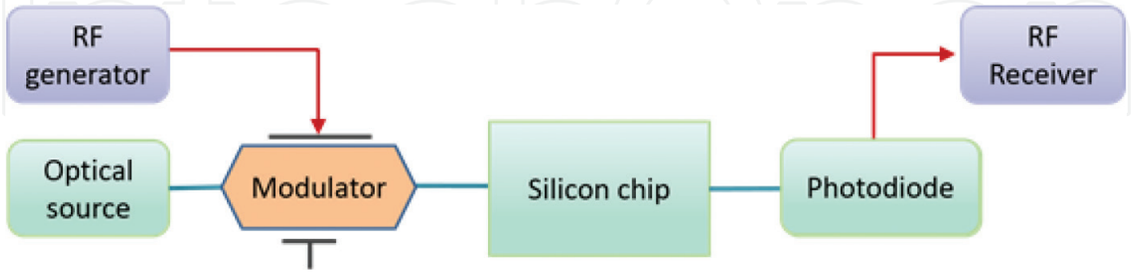


Figure 2. Schematic illustration of chip-scale microwave photonic signal processing.

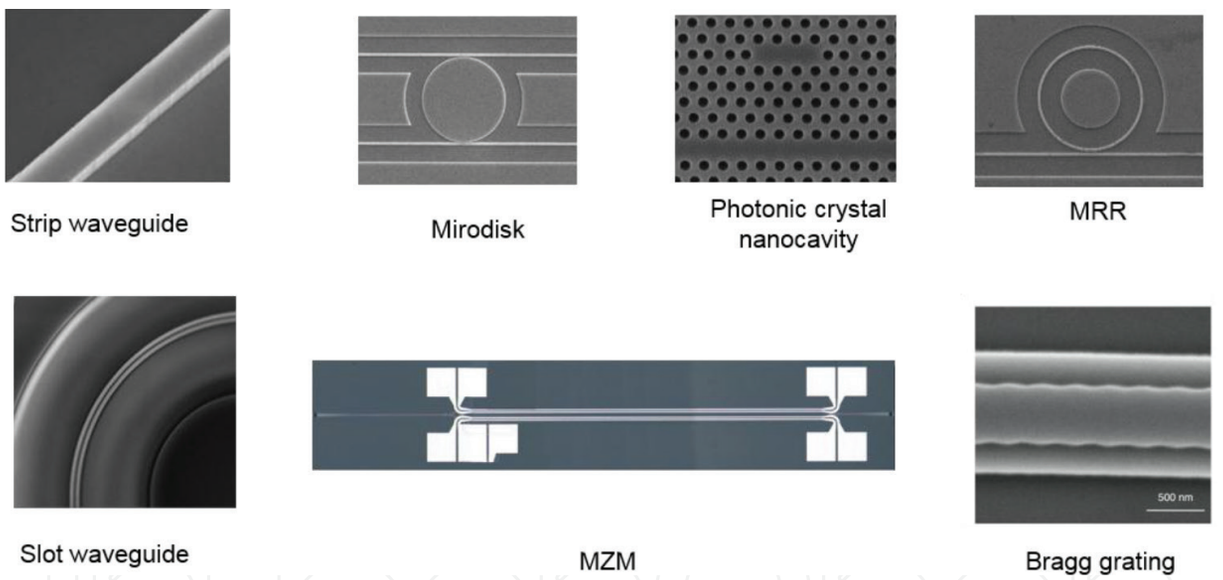


Figure 3. Some photographs of basic silicon photonic devices for MWP signal processing. (The photograph of Bragg grating is reprinted from Ref. [70]).

2. On-chip analog signal transmission

All the MWP systems are essentially analog links. For an analog optical link, linearity is one of the key performance metrics. Traditionally, there are mainly three methods to increase the linearity of analog signal transmission in various systems: (1) improving the driving/bias schemes or optical structures of the modulators to construct linear or quasi-linear modulators [71–74]; (2) using a tunable filter with proper center wavelength and bandwidth to remove the unwanted optical carrier and thus rise the linearity of analog links [75, 76]; (3) using

optical waveguides with extremely low nonlinearity, low-loss and high thermal stability for signal transmission [77]. Integrated silicon photonic devices such as silicon waveguides, MRR, microdisk resonators, and PhC cavities have promoted the evolution of on-chip MWP signal processing functions due to the high nonlinear effects of waveguides and diverse filtering properties of resonators. However, these characteristics may also degrade analog signal quality awfully, leading to extra nonlinear signal distortions, which may show different properties compared with traditional signal distortions. To investigate the impacts on analog optical links induced by the nonlinearity of integrated photonic devices, many interesting and meaningful works related to on-chip analog performance have been done recently [53, 54, 78–81]. In this section, we analyze the performance of on-chip analog signal transmission using silicon waveguide, MRR, and PhC nanocavity.

For an on-chip analog link, silicon waveguide is used for light routing. Compared to fiber-based links, the optical nonlinearities induced by the tight light confinement of the silicon waveguides may affect the performance of on-chip analog photonic links. So it is essential to experimentally exploit analog signal transmission distortions induced by the integrated silicon waveguide for future chip-scale analog systems. The experimental setup for analog signal transmission through the fabricated silicon strip waveguide is shown in **Figure 4**. At the transmitter side, the output of an external cavity laser (ECL) is injected to a MZM. Two microwave at frequencies f_1 = 1.98 GHz and f_2 = 2 GHz are combined at the input of MZM. The light source is modulated by the two RFs in the MZM. **Figure 4(a)** and **(b)**describes the typical RF signals at the input and output of MZM. A 1550-nm source emitted from the ECL is modulated by MZM, and then amplified by an erbium-doped fiber amplifier (EDFA). A variable optical attenuator (VOA) is employed to control the optical input power of the silicon strip waveguide. The analog signals are polarization controlled by using a polarization controller (PC), and then coupled into the silicon strip waveguide by vertical grating coupler from fiber. For the dimensions confinement of the SOI wafer, there is a bending region of the long waveguide and the scanning electron microscope (SEM) image of the waveguide bending region is shown in **Figure 4(c)**. **Figure 4(d)** depicts the field distribution of the fundamental mode in silicon strip waveguide calculated by using a full-vector finite-element-method software (COMSOL). After transmission through the silicon strip waveguide, the analog signal is coupled out from the silicon strip waveguide to fiber with the same vertical grating coupler. An electrical spectrum analyzer (ESA) is used to measure the fundamental, second-order harmonic distortion (SHD), third-order harmonic distortion (THD), second-order intermodulation (IM2), and third-order intermodulation (IM3) products.

Figure 5 shows the measured signal-to-noise ratios (SNRs) of IM2, IM3, SHD, and THD as a function of the silicon strip waveguide length. The waveguide length we fabricated is 1, 3.23, 5.25, and 7.38 mm, respectively. One can see that the SNRs of distortions have a negligible change with the increase of the waveguide length.

Figure 6 shows the measured SNRs of IM2, IM3, SHD, and THD as a function of optical input power fed into the silicon strip waveguide. One can see that the SNRs of IM2, IM3, and SHD have a negligible change when increasing the optical input power. The SNR of the THD gradually increases with the input optical power, which might be due to the relatively high sensitivity of THD to the nonlinearity-induced degradation of the silicon strip waveguide.

http://dx.doi.org/10.5772/66322

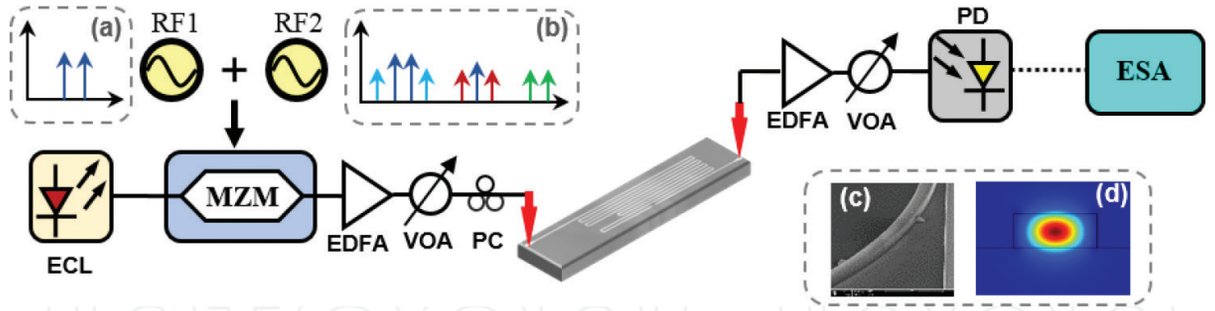


Figure 4. Experimental setup for analog signal transmission through the silicon strip waveguide. Insets: (a) and (b) describe the RF signal at the MZM input and output; (c) is the SEM image and (d) is the simulated mode distribution of silicon strip waveguide.

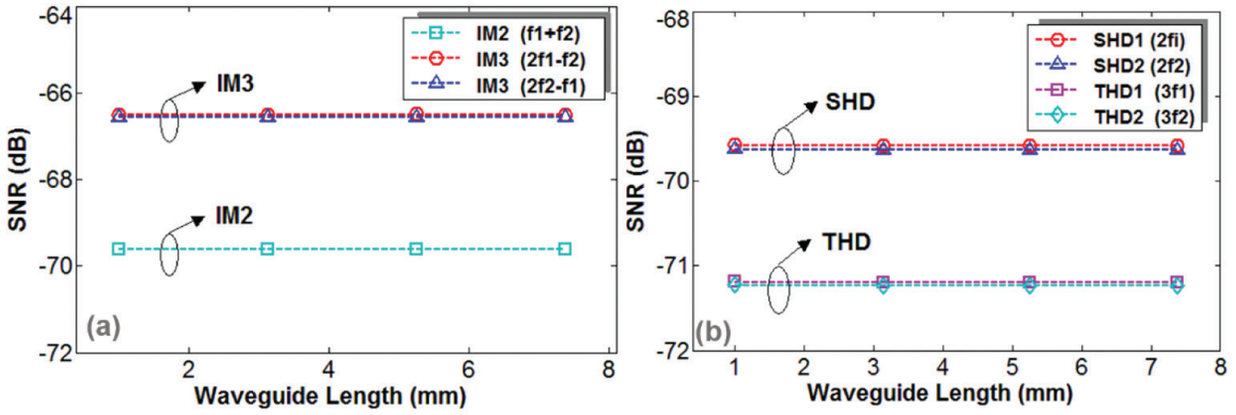


Figure 5. Measured SNRs of (a) IM2, IM3 and (b) SHD, THD versus waveguide length.

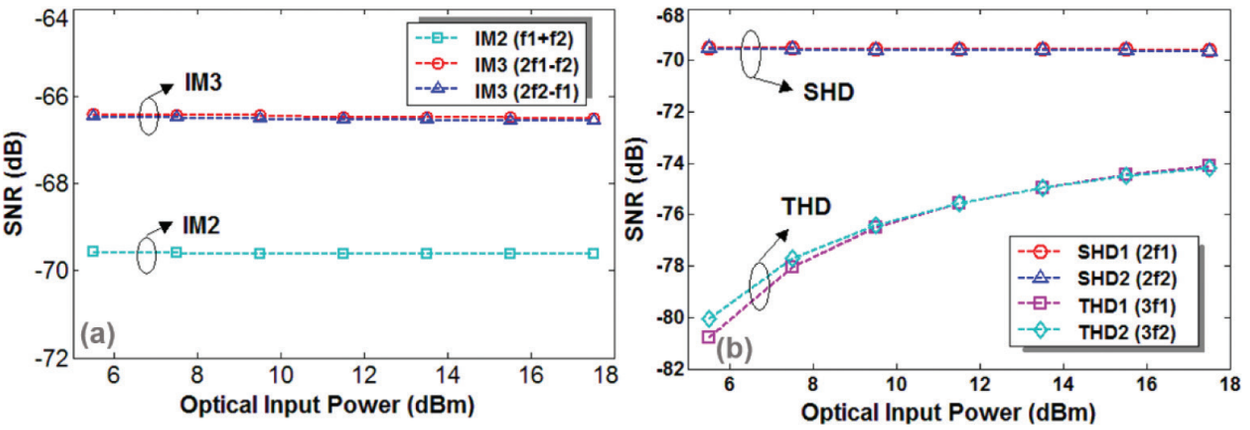


Figure 6. Measured SNRs of (a) IM2, IM3 and (b) SHD, THD versus optical input power.

We then evaluate the performance of on-chip analog signal transmission in a silicon MRR [53]. **Figure 7** shows the experimental setup. At the transmitter, the output of an ECL is sent to a MZM driven by a 6-GHz RF signal. The analog signal is amplified by an EDFA, polarization controlled by a PC, and then adjusted by a VOA. With a vertical grating coupler, the analog

signal is coupled from fiber to silicon microring resonator. After the transmission through a silicon microring resonator, at the receiver, the signal is coupled from the silicon microring resonator to fiber with a vertical grating coupler. After being amplified by EDFA and attenuated by VOA, the signal is sent to a photodetector (PD) and then measured by an ESA. The insets (a) and (b) in **Figure 7** depict the SEM images of the fabricated vertical grating coupler and silicon microring resonator. In the experiment, the silicon microring resonator has a resonance wavelength of ~1581.26 nm and a 3-dB bandwidth of ~0.12 nm.

Figure 8(a) and **(b)** shows the acquired output power of the RF carrier and distortions as a function of the RF input power at input signal wavelength of ~1581.07 and ~1581.21 nm, respectively.

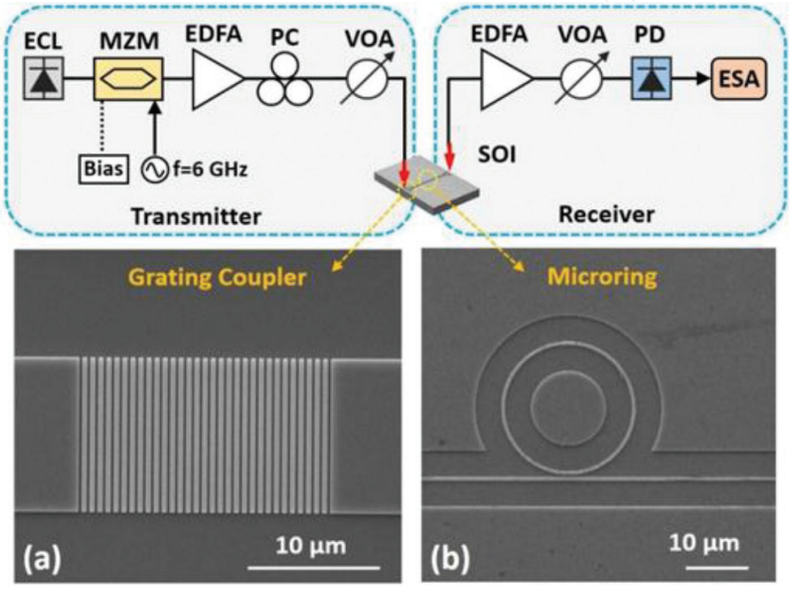


Figure 7. Experimental setup for analog signal transmission in a silicon microring resonator. (a) and (b) SEM images of the grating coupler and silicon microring resonator, respectively.

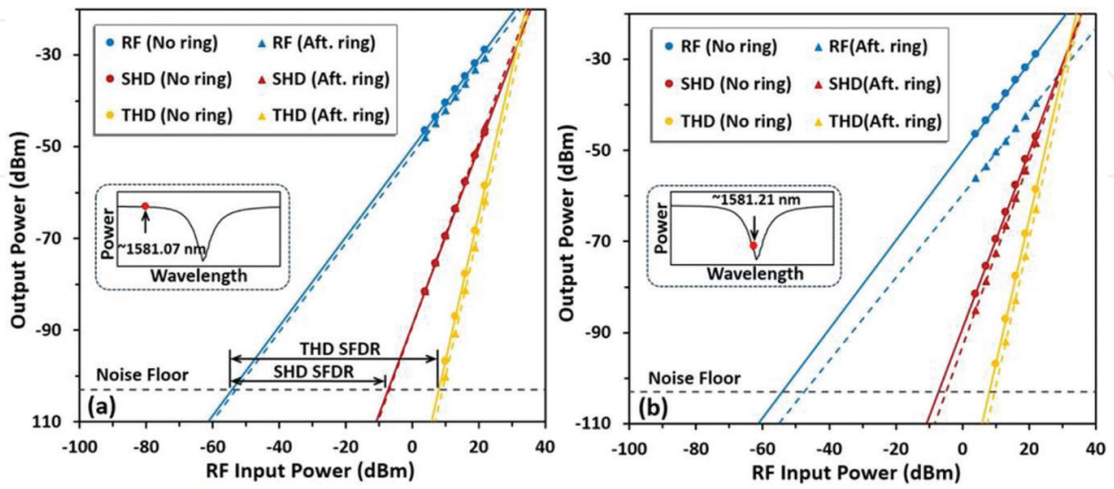


Figure 8. Measured output power of RF carrier and distortions as a function of the RF input power at input signal wavelength of (a) 1581.07 nm and (b) 1581.21 nm, respectively. The optical power of input signal is −17 dBm.

The spurious-free dynamic range (SFDR) of the SHD and THD are used to estimate the analog link performance. A higher SFDR system facilitates a more linear analog signal transmission. As shown in **Figure 8(a)**, for input signal wavelength of 1581.07 nm which is away from the dip resonance wavelength, the output power of RF carrier and distortions after microring change slightly compared with those without microring. The resultant SHD and THD SFDR after microring almost remain the same as those without microring. As shown in **Figure 8(b)**, for input signal wavelength of 1581.21 nm which is close to the dip resonance wavelength, the output power of RF carrier decreases while the distortions vary slightly after microring compared with those without microring. Hence, the SHD and THD SFDR decrease after the transmission, which is due to the notch filtering effect of the silicon microring resonator around the dip resonance wavelength.

To further investigate the analog signal transmission in the 3-dB bandwidth region near the resonance wavelength of 1581.26 nm, we change input signal wavelength from ~1581.07 to ~1581.26 nm with a 0.048-nm spacing. **Figure 9(a)** plots the relationship between SFDR and input signal wavelength at input signal power of 3.5 dBm. One can see two interesting phenomena from **Figure 9(a)**. First, although the minimum optical power transmission wavelength (i.e., notch resonance wavelength) is at ~1581.26nm, the worst SFDRs are obtained at ~1581.21 nm due to the notch filtering effect on the RF carrier sideband. Second, SFDRs at ~1581.12 nm achieve maximum values, which can be explained with the fact that the high-order harmonic sidebands (output SHD and THD) fall into the 3-dB bandwidth region (close to the notch resonance), while the fundamental frequency sideband (output RF carrier) is away from the notch resonance. For low-level input signal power, it is found that the analog signal transmission performance through microring resonator is mainly affected by the notch filtering effect. Input signal power is also taken into consideration to assess its role in the analog signal transmission, as shown in **Figure 9(b)**. For relatively high input signal power, it is interesting to note that the analog signal transmission might be affected by the nonlinearity-induced resonance wavelength shift of the microring with the increase of input signal power.

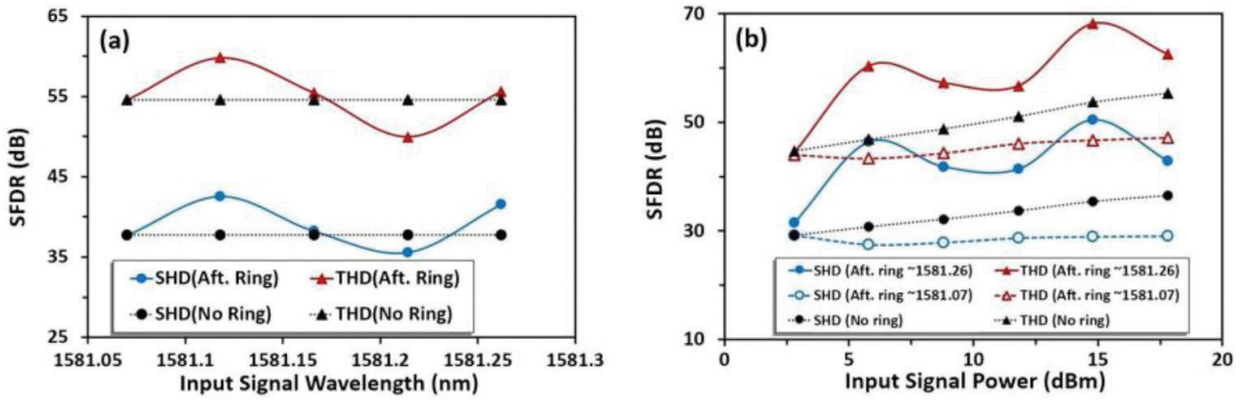


Figure 9. (a) Measured SHD and THD SFDR versus input signal wavelength at input signal power of 3.5 dBm. (b) Measured SHD and THD SFDR versus input signal power.

We further assess the performance of on-chip analog signal transmission using the fabricated silicon photonic crystal nanocavities [54]. The designed and fabricated silicon photonic crystal nanocavity is shown in **Figure 10**. The lattice constant (a) is 420 nm, the radius of air holes (r)

is 126 nm, and the three air holes adjacent to the cavity are laterally shifted by 0.175a, 0.025a, and 0.175a, respectively. In the experiment, the silicon photonic crystal nanocavity has a resonance wavelength of ~1552.99 nm, an extinction ratio of ~18.4 dB, and a 3-dB bandwidth of ~0.19 nm.

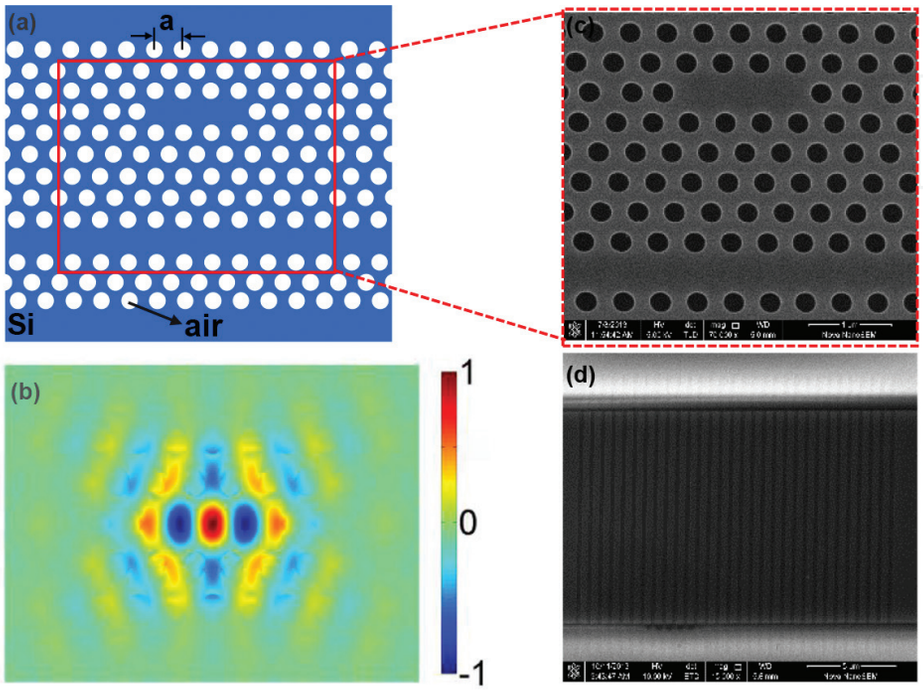


Figure 10. (a) Structure, (b) mode profile and (c) SEM image of silicon photonic crystal nanocavity. (d) SEM image of vertical grating coupler.

Figure 11(a) and **(b)**shows the measured output power of the RF carrier and distortions (SHD, THD) as a function of the RF input power at input optical carrier wavelength of 1552.83 and 1552.99 nm, respectively. As shown in **Figure 11(a)**, for input optical carrier wavelength of 1552.83 nm, the SHD SFDR (~29.8 dB) and THD SFDR (~50.0 dB) degrade slightly. As shown in **Figure 11(b)**, for input optical wavelength of 1552.99 nm (i.e., resonance wavelength), slight degradations of SHD SFDR (~34.6 dB) and THD SFDR (~52.2 dB) are observed. Actually, when the optical carrier is tuned at the resonance wavelength, the modulated optical sidebands after MZM (RF modulation), which are related to the RF carrier and distortions (SHD, THD), are offset from the dip resonance wavelength. As a result, it might not be the worst case for analog signal transmission with the optical carrier sitting at the resonance wavelength of the photonic crystal L3 resonator.

The influences of the optical carrier wavelength and input optical power on the SHD SFDR and THD SFDR are also studied in the experiment. **Figure 12(a)** shows the dependence of SHD SFDR and THD SFDR on the input optical carrier wavelength. **Figure 12(b)** shows the dependence of SHD SFDR and THD SFDR on the optical input power. The obtained results shown in **Figures 11** and **12** indicate favorable analog link performance using the designed and fabricated silicon photonic crystal L3 resonator.

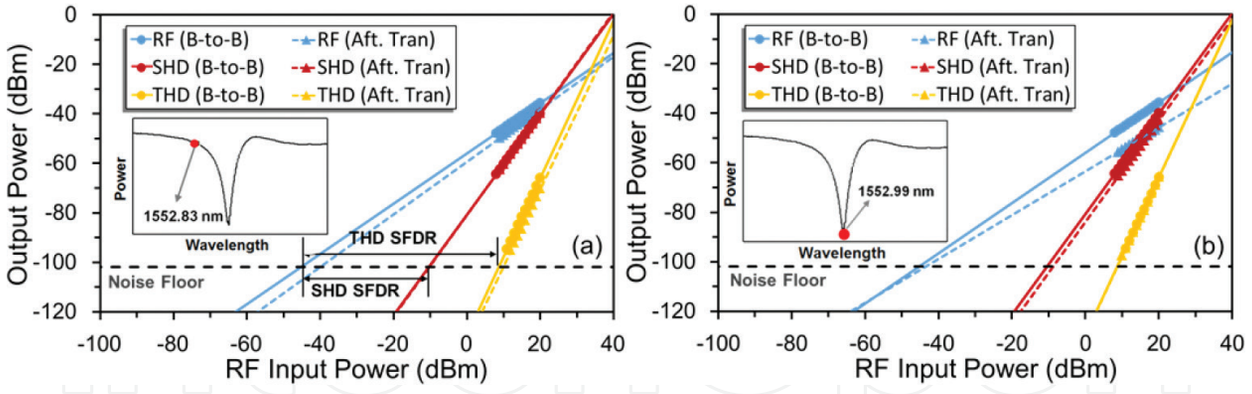


Figure 11. Measured output power of RF carrier and distortions (SHD, THD) as a function of RF input power at different optical carrier wavelengths of (a) 1552.83 and (b) 1552.99 nm.

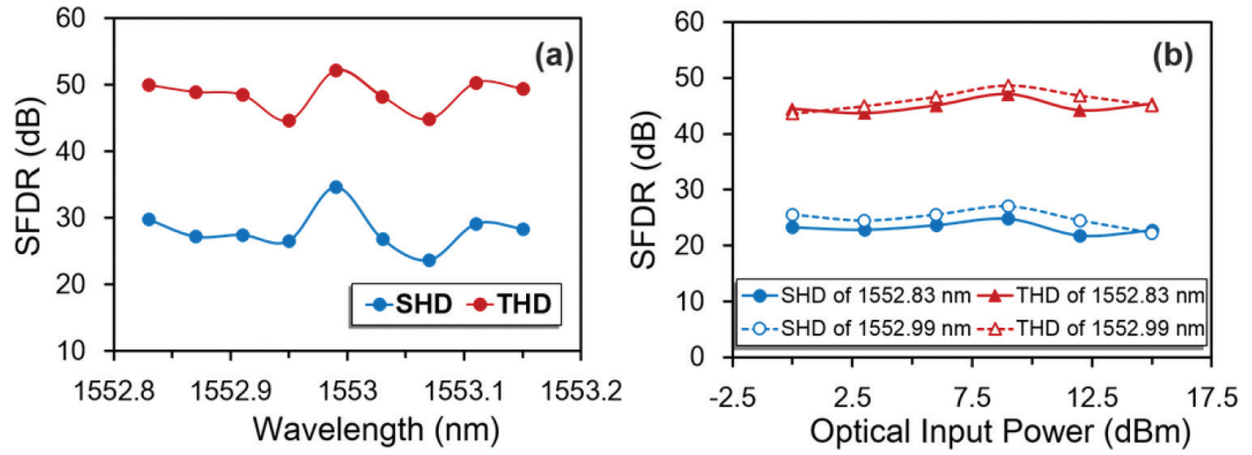


Figure 12. Measured output power of RF carrier and distortions (SHD, THD) as a function of RF input power at different optical carrier wavelengths of (a) 1552.83 and (b) 1552.99 nm.

3. Microwave photonics filters

A MWP filter is a photonic subsystem designed with the aim of carrying equivalent tasks to those of a traditional microwave filter within a RF system [35, 82–85]. Comparing to conventional microwave filters, MWP filters have attracted increasing interest for their advantages, such as huge bandwidth, electromagnetic immunity as well as reconfiguration and tunability. Now, MWP filters are used broadly ranging from radar, satellite to wireless communications. Many approaches to realizing MWP filters have been proposed and demonstrated based on fiber devices in the last decade [86–91]. To enhance the stability and reduce the cost and footprint of the MWP filters, integrated MWP filters have been widely concerned by several groups recently [41, 44, 47, 92–99]. Many of the preliminary approaches have been based mainly on single integrated cavity resonators. For instance, Ref. [96] reports the results for a single passband MWP filters based on a silicon MRR. A few works have also focused on more elaborated designs involving more than one cavity, such as cascaded MRRs [94], MZI-assisted MRRs [41], and more. In this section, we introduce various types of MWP filters.

Using a silicon MRR assisted by a phase modulator (PM) and a tunable optical filter (TBF) to prepare an optical single sideband (OSSB) modulation signal, we demonstrate a bandstop microwave photonic filter [42]. Moreover, using light (pump) to control light (signal optical carrier), we present an alternative approach to tuning the resonance of the bandpass microwave photonic filter, that is, all-optical tuning microwave photonic filter. **Figure 13(a)** illustrates the typical scheme of the all-optical tuning process of the MWP filter based on an SOI MRR. The microwave signal is modulated on a signal optical carrier, and then processed by an SOI MRR and detected by a PD. Since the optical response of the MRR can be adjusted by a pump light, the electrical response of the link can be tuned. The inset of **Figure 13(a)** depicts typical transmission spectrum of an SOI MRR, in which the microwave-modulated signal is located close to one notch resonance frequency and pump light positioned at another notch

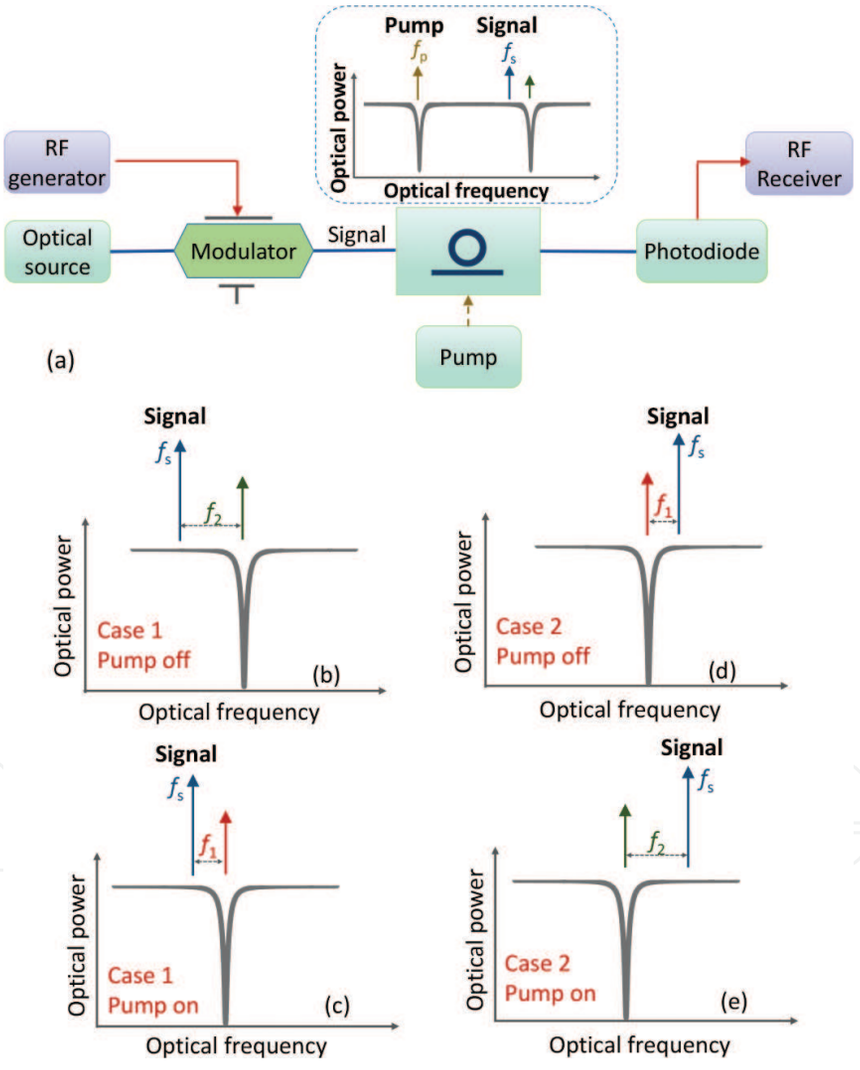


Figure 13. (a) Schematic illustration of the proposed all-optical tuning process of the MWP filter. (b)–(e) Operation principle of the all-optical tuning process of the MWP filter. (b) and (d) Pump off. (c) and (e) Pump on. Case 1: the frequency of the signal optical carrier (fs) is located at the left side of the notch resonance frequency of the MRR. Case 2: the frequency of the signal optical carrier (fs) is located at the right side of the notch resonance frequency of the MRR. The inset of (a) shows typical transmission spectrum of the MRR with relative positions of microwave modulated signal and pump light.

resonance frequency. **Figure 13(b)–(e)** summarizes the operation principle of the proposed all-optical tuning process of the MWP filter. An optical carrier is modulated by an RF signal with OSSB modulation. The output field after modulation is then applied to the MRR for microwave photonic signal processing. The frequency of the signal optical carrier is f_s. There are two cases depending on the relative position between the signal optical carrier and the notch resonance of the MRR. For the Case 1 with the signal optical carrier f_s located at the left side of the notch resonance of the MRR, when the frequency component ($f_s + f_2$) is just aligned to the notch frequency of the MRR spectrum as shown in **Figure 13(b)**, the output RF response in the absence of the pump vanishes at f_2. Hence, a notch MWP filter with a central frequency of f_2 is obtained. When the pump light is on, one would expect a red shift of the notch peak of the MRR owing to the combined nonlinear effects in the MRR, resulting in a notch MWP filter with a central frequency of f_1, as shown in **Figure 13(c)**. Hence, the central frequency of the notch MWP filter can be tuned from f_2 to f_1 by increasing the pump light power. For the Case 2 with the signal optical carrier f_s located at the right side of the notch resonance of the MRR, as shown in **Figure 13(d)** and **(e)** similar tunable notch MWP filter with its central frequency changed from f_1 to f_2 is also achievable by increasing the pump light power. Both Case 1 and Case 2 shown in **Figure 13(b)–(e)** indicate possible all-optical tunale MWP filter using nonlinear effects of MRR.

We first calculate the RF responses under different pump light power to show the all-optical tuning process of the MWP filter. The parameters used to calculate MRR field transmission are extracted from the measured MRR transmission spectrum. The MWP filter responses under different pump powers in Case 1 and Case 2 are shown in **Figure 14(a)** and **(b)**, respectively. As shown in **Figure 14(a)**, the central frequency of the MWP filter decreases from 15.5 to 9.5 GHz as the pump power increases in Case 1. The central frequency of the MWP filter increases from 9.5 to 15.5 GHz as the pump power increases in Case 2, as shown in **Figure 14(b)**.

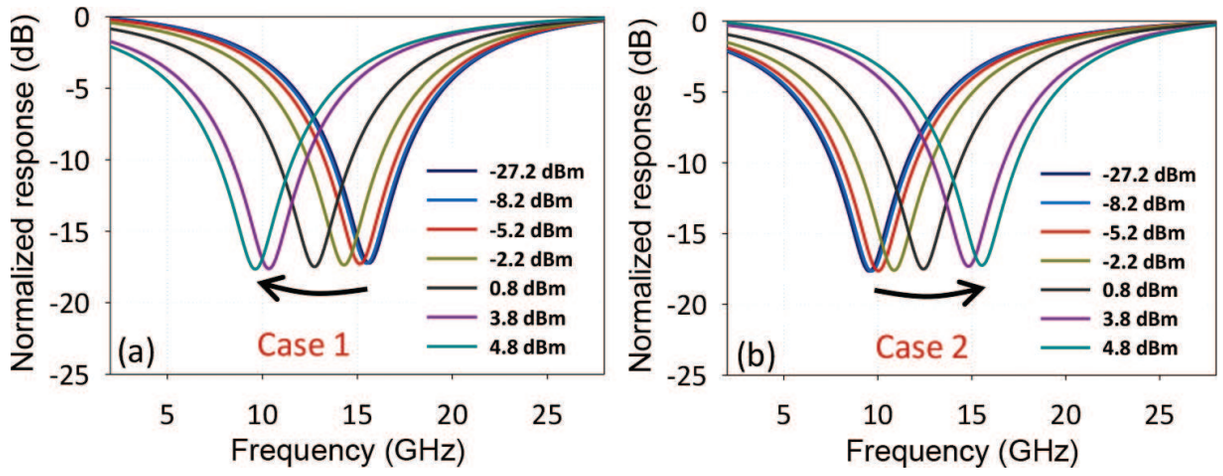


Figure 14. Calculated microwave responses under different pump power levels in (a) Case 1 and (b) Case 2, respectively. Case 1: the central frequency of the MWP filter decreases as the pump power increases. Case 2: the central frequency of the MWP filter increases as the pump power increases.

The measured microwave responses of MWP filter under different pump power levels are shown in **Figure 15**. The pump light wavelength is fixed at 1591.786 nm for all the configurations.

In Case 1, the optical carrier wavelength is 1581.730 nm in both forward and backward pumping configurations. As shown in **Figure 15(a)** and **(b)**, the central frequency of the notch MWP filter is tuned from 15.64 to 8.79 GHz in the forward pumping configuration while from 15.60 to 10.04 GHz in the backward pumping configuration by adjusting the pump light power from −27.2 to 4.8 dBm. In Case 2, the optical carrier wavelength is 1581.564 nm in the forward pumping configuration and 1581.534 nm in the backward pumping configurations. As shown in **Figure 15(c)** and **(d)**, the central frequency of the notch MWP filter is tuned from 5.27 to 12.47 GHz in the forward pumping configuration and from 8.84 to 15.04 GHz in the backward pumping configuration as increasing the pump light power from −27.2 to 4.8 dBm.

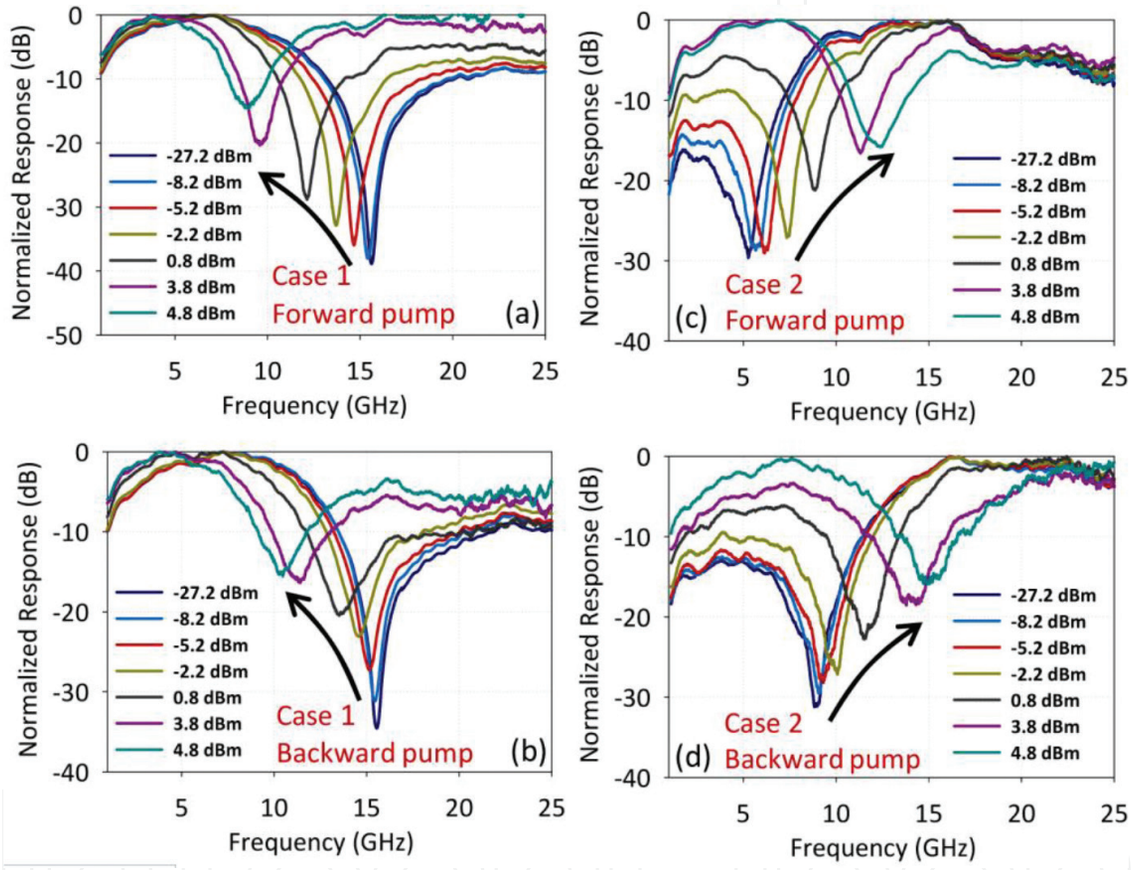


Figure 15. Measured microwave responses of all-optical tunable MWP filter under different pump power levels with (a) Case 1/Forward pump, (b) Case 1/Backward pump, (c) Case 2/Forward pump, and (d) Case 2/Backward pump, respectively.

We also propose a simple yet effective approach to realizing notch MWP filter with an ultra-high peak rejection [43]. We use the combination of a PM, TBF, and an SOI MRR to manipulate the phase and amplitude of optical sidebands for inducing a signal cancellation at the RF notch filter frequency. **Figure 16** shows the concept and operation principle of the proposed approach. A conventional PM driven by an RF signal generates out of phase lower sideband (LSB) and upper sideband (USB). A TBF is used to attenuate the USB signal followed by an SOI MRR. The resonant frequency of the SOI MRR is aligned to the frequency of LSB signal, thus the LSB signal will be filtered by the SOI MRR. Since the SOI MRR has a limited extinc-

tion ratio, the amplitude of the remaining LSB signal could be equal to the USB signal. Due to the equal amplitude and π phase difference of the attenuated USB and remained LSB, the signal power at the modulated RF frequency can be cancelled after detection by a photodetector, and a notch microwave photonic filter with infinite rejection in principle can be achieved.

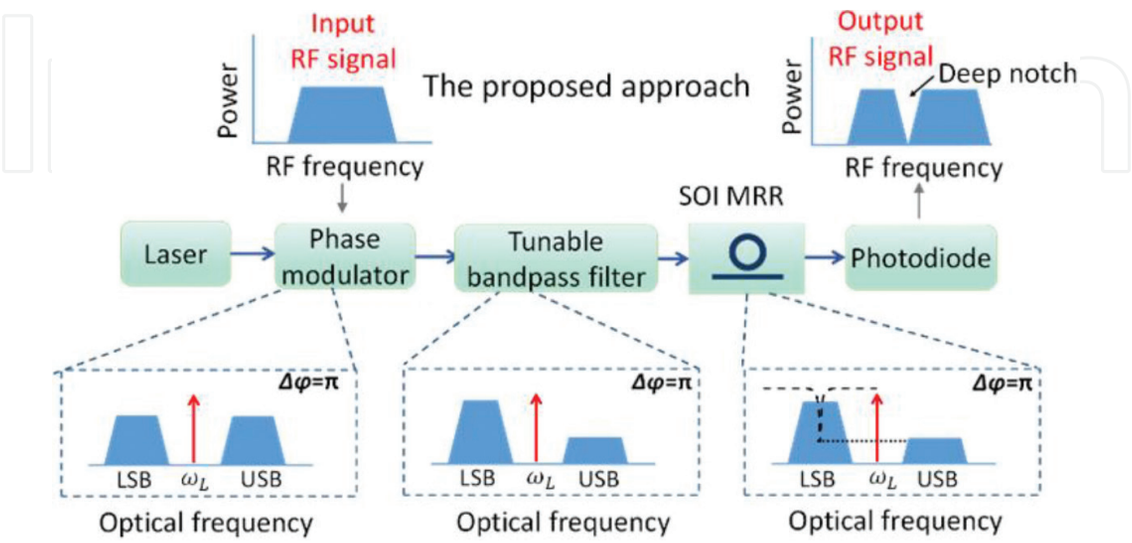


Figure 16. Schematic illustration of the proposed notch MWP filter with ultra-high peak rejection.

The measured optical spectra after the TBF and the corresponding MWP filter responses are shown in **Figure 17**. The optical carrier wavelength is 1581.576 nm. The optical spectra are measured by modulating a microwave signal to the optical carrier. The frequency of the microwave signal is 20 GHz, which is comparable with the central frequency of the MWP filter. **Figure 17(a)–(d)** depicts the optical spectra when the central wavelength of the TBF is 1581.746, 1581.776, 1581.806, and 1581.836 nm, respectively. The transmission spectra of the TBF in these four cases are also plotted in **Figure 17(a)–(d)** for reference. **Figure 17(e)–(h)** shows the corresponding MWP filter responses. As shown in **Figure 17(a)** and **(d)**, when the USB component is slightly attenuated by the TBF, after passing through the MRR, the amplitude difference of the LSB and USB is relatively large, resulting in a shallow RF notch of about 14.5 dB. When we shift the TBF, more power of the USB component is attenuated, and the peak rejection of the MWP filter remarkably increases. The peak rejection of the MWP filter is 29.1 dB when the central wavelength of the TBF is 1581.776 nm as shown in **Figure 17(b)** and **(f)**. A maximum peak rejection of about 61.5 dB is observed with balanced amplitude between LSB and USB components when the central wavelength of the TBF is 1581.806 nm as shown in **Figure 17(c)** and **(g)**. When we further increase the central wavelength of the TBF, the USB signal will be further attenuated, thus the peak rejection decreases again. For example, when the central wavelength of the TBF is 1581.836 nm, the USB almost disappears, and the peak rejection of the MWP filter decreases to 40.9 dB as shown in **Figure 17(d)** and **(h)**.

By changing the carrier light wavelength, the operating frequency of the ultra-high peak rejection MWP filter can be tuned. We measure the operating frequency tunability of the

MWP filter, as shown in **Figure 18**. When the wavelength of the carrier light is changed from 1581.476 to 1581.626 nm, the central frequency of the MWP filter is tuned from 12.4 to 30.6 GHz, maintaining an ultra-high peak rejection. The obtained results shown in **Figure 18** indicate that the proposed ultra-high peak rejection MWP filter can operate over a large tunable frequency range.

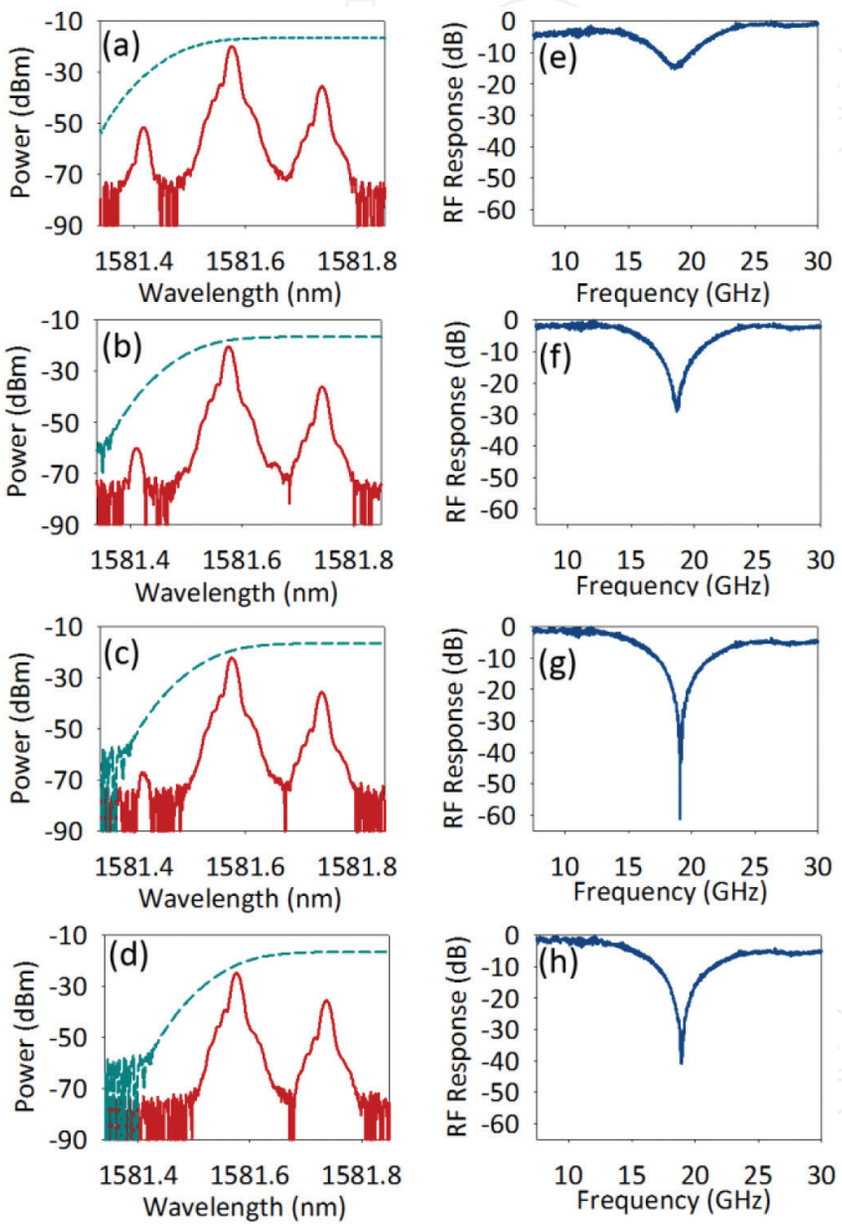


Figure 17. (a)-(d) Optical spectra after the TBF when the central wavelength of the TBF is 1581.746, 1581.776, 1581.806, and 1581.836 nm, respectively. The dashed lines are the corresponding transmission spectrum of TBF. (e)–(h) The corresponding MWP filter responses.

Based on a similar principle, we also demonstrate a rejection ratio tunable notch MWP filter based on a silicon PhC nanocavity. The resonant wavelength of the cavity is around 1554.313 nm. The measured optical spectra after the TBF and the corresponding MWP filter responses are shown

in **Figure 19**. The carrier light wavelength is 1554.153 nm. **Figure 19(a)–(d)** depicts the optical spectra when the central wavelength of the TBF is 1554.262, 1554.292, 1554.322, and 1554.352 nm, respectively. **Figure 19(e)–(h)** shows the corresponding MWP filter responses. The experimental results agree well with the simulation. As shown in **Figure 19(a)** and **(e)**, when the USB signal is slightly modified by the TBF, the peak rejection of the obtained MWP filter is very small (~11.8 dB). When we shift the TBF, the power of USB signal decreases, and the peak rejection of the MWP filter increases. A maximum peak rejection of about 62.1 dB is observed when the central wavelength of the TBF is 1551.315 nm (**Figure 19(b)** and **(f)**). When we further increase the central wavelength of the TBF, the USB signal will be further attenuated, thus the peak rejection will decrease again. For example, as shown in **Figure 19(d)** and **(h)**, the peak rejection of the MWP filter decreases to 15 dB when the central wavelength of the TBF is 1551.375 nm. **Figure 19(i)** plots the rejection ratio as a function of the central wavelength of the TBF. The red curve shows the simulation data, while the experimental results are marked by blue circles.

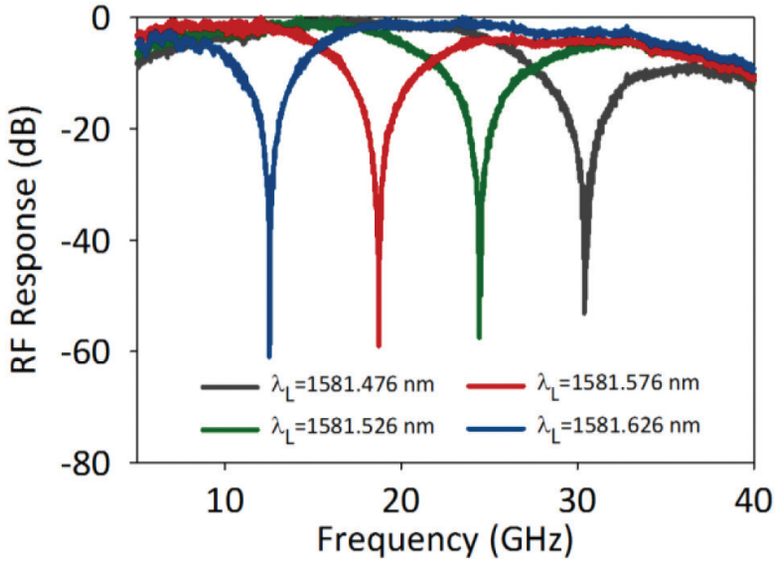


Figure 18. Measured tunable ultra-high peak rejection MWP filter responses with different optical carrier wavelengths.

To evaluate the effect of the filter shape of TBF, we study the performance of the rejection ratio tunable MWP filter with four types of super-gaussian filter shape. We calculate the MWP filter tunability response when the transmission of the TBF is $T_{TBF}(\omega) = e^{-\left(\frac{\omega-\omega_{center}}{2\pi\times 34.89\times 10^9}\right)^N}$ $(N = 2, 4, 6, 8)$. **Figure 20(a)** shows the rejection ratio of the MWP filter as a function of TBF central wavelength with different filter shapes of TBF. To show the operation stability in high rejection ratio region with different TBF filter shapes, we define the TBF central wavelength tolerance as operation span of TBF central wavelength when the rejection ratio is greater than 40 dB. **Figure 20(b)** plots the TBF tolerance of central wavelength with different filter shapes of TBF. It can be seen that higher-order super-gaussian function leads to worse stability of the system.

Since the high nonlinearities induced by the tight light confinement of silicon photonic devices, the influence of optical nonlinear effects should also be taken into consideration

when designing MWP devices. MWP devices such as MWP filters based on silicon waveguide devices might have strong nonlinear microwave responses, which are dependent on the optical carrier power level. Taking the PhC microcavity as an example, we study the nonlinear microwave responses of the MWP filters based on the SOI waveguide devices.

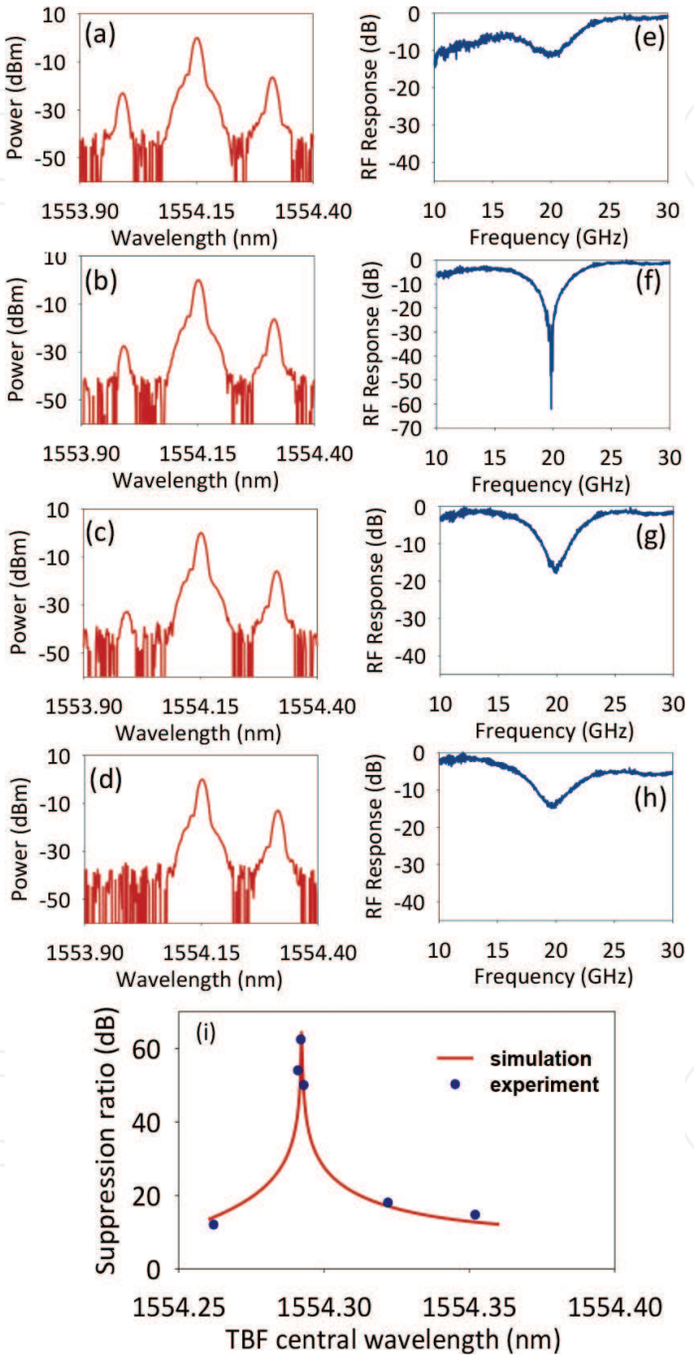


Figure 19. (a)–(d) Optical spectra after the TBF when the central wavelength of the TBF is 1554.262, 1554.292, 1554.322, and 1554.352 nm, respectively. (e)–(h) The corresponding MWP filter response. (i) Rejection ratio as a function of TBF central wavelength.

Figure 21(a) illustrates the typical scheme of an MWP filter based on a PhC microcavity. **Figure 21(b)** and **(c)** summarizes the operation principle of the device. After been phase

modulated, the output field is then sent to a PhC microcavity. Assuming that the wavelength of optical carrier is λ_c, locating on the left side of the linear notch resonant wavelength of the PhC microcavity (Case 1), as shown in **Figure 21(b)**, when the optical carrier power is very low and one of the sideband (f_1) is just aligned to the notch resonant wavelength of the PhC microcavity, a bandpass MWP filter with a central frequency of f_1 is obtained. When the optical carrier power is increased, considering the combined nonlinear effects in the PhC microcavity, the notch peak of the microcavity will red shift (e.g., shift by f_2-f_1), resulting in an bandpass MWP filter with a varied central frequency of f_2. When the wavelength of optical carrier is located on the right side of the linear notch resonant wavelength of the PhC microcavity, the situation is a little more complicated. For Case 2, as shown in **Figure 21(c)**, the initial notch peak of the PhC microcavity is aligned to the left sideband corresponding to f_2. When the optical carrier power is increased, the notch peak wavelength will red shift, leading to the decrease of the central frequency of the MWP filter. Remarkably, when we further increase the optical carrier power, the notch peak will go across the optical carrier wavelength. Hence, the central frequency of the MWP filter will first decrease and then increase when gradually increasing the optical carrier power from a very low level to a relatively high level.

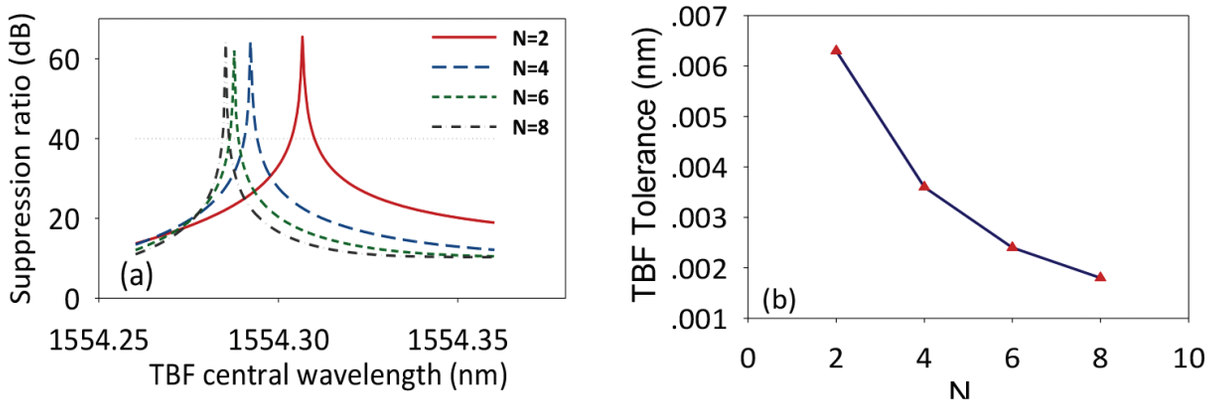


Figure 20. (a) Rejection ratio as functions of TBF central wavelength with different filter shape of TBF. (b) TBF tolerance of central wavelength with different filter shape of TBF.

The resonant wavelength of the cavity is around 1554.152 nm. **Figure 22** shows measured MWP filter responses under different optical carrier power levels for Case 1 and Case 2. The wavelengths of the carrier are 1554.056 and 1554.296 nm, respectively. For Case 1, since the notch resonant wavelength of the PhC microcavity red shifts as the optical carrier power increases, the central frequency of the MWP filter increases. When the optical carrier power increases from −13.5 to 5.5 dBm, the central frequency of the MWP filter is changed from 13.9 to 24 GHz. For Case 2, when the optical carrier is increased from −13.5 to −3.5 dBm, the central frequency of the MWP filter decreases, which indicates that the resonant wavelength of the PhC microcavity is still on the left side of the optical carrier in the process. When we increase the power from −3.5 to −1.5 dBm, the central frequency of the MWP filter suddenly jumps to another frequency at about −2 dBm. When we further increase the power of the carrier light, the central frequency of the MWP filter increases, in contrast with the decrease in low-power region. The obtained results here indicate that the resonance of the

PhC microcavity first jumps to the right side of the carrier, and then red shifts as the carrier further increases.

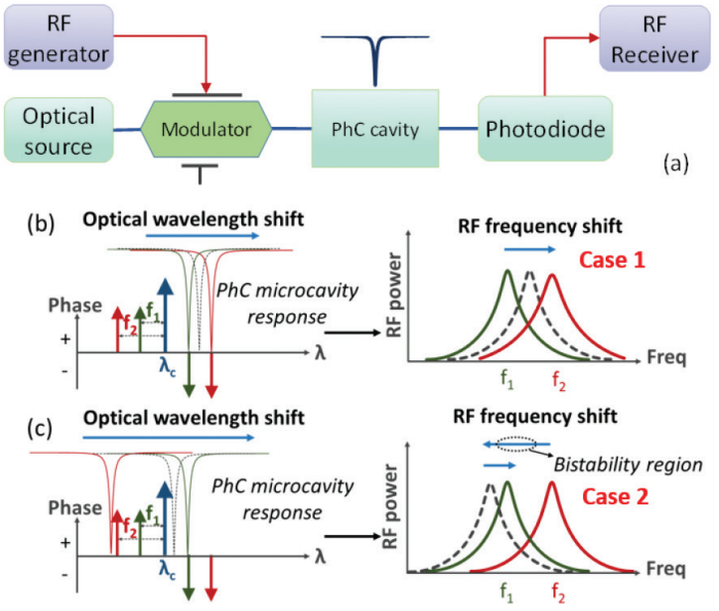


Figure 21. (a) Schematic illustration of the typical scheme of a MWP filter based on PhC cavity. (b) and (c) Working principle of the optical carrier power dependent MWP filter. Case 1: the wavelength of the optical carrier is located on the left side of the linear notch resonant wavelength of the PhC microcavity. Case 2: the wavelength of the optical carrier is located on the right side of the linear notch resonant wavelength of the PhC microcavity.

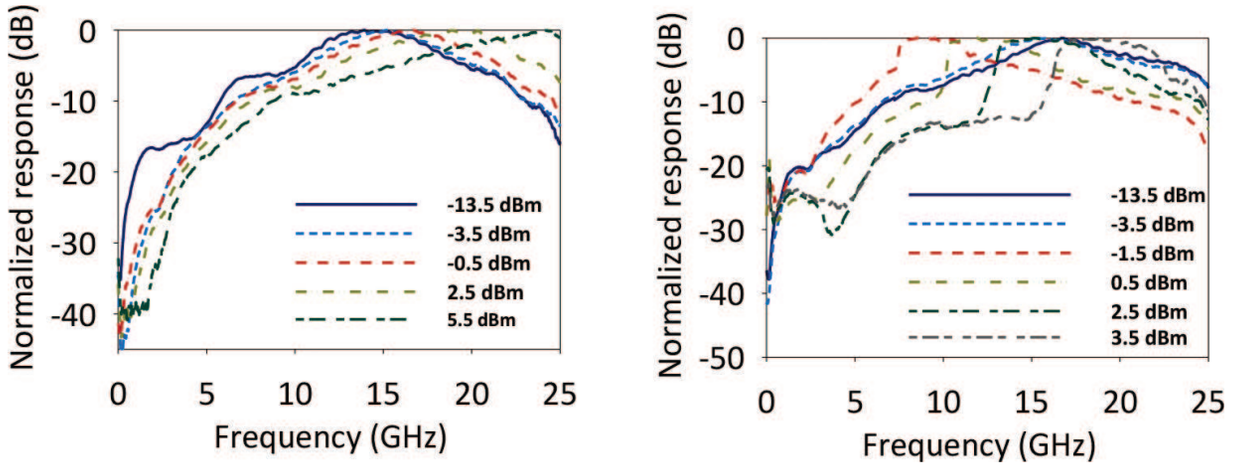


Figure 22. Measured MWP filter responses under different optical carrier power levels for (a) Case 1 and (b) Case 2.

4. Photonic-assisted microwave signal multiplication and ASK modulation

Photonic-assisted generation of microwave signals can find interesting applications in many microwave photonic systems, such as broad-band wireless access networks, software-defined radio, antenna remoting, phased-array antenna, and radar systems [65]. Usually,

optical microwave generation is based on heterodyne techniques. Several approaches to generating two phase-correlated optical waves have been proposed and demonstrated based on free space devices [100, 101] and fiber devices [64, 65, 102–111]. Among these approaches, microwave frequency multiplication based on external modulation using MZMs has been considered an effective solution for high frequency and tunable microwave signal generation. Photonic generation of RF binary digital modulation signals is another key technology in microwave photonics. Amplitude-shift keying (ASK), phase-shift keying (PSK), and frequency-shift keying (FSK) are basic modulation formats in wireless communications, which convey information by modulating the amplitude, phase or frequency of a continuous carrier wave. Traditionally, these modulation microwave signals are generated in electrical domain using digital electronic circuits [40]. Due to the electronic bottleneck, the major difficulty of this traditional technique is that the frequency of the generated signals is limited to a few gigahertz. An effective method to generate high frequency RF signals is to generate RF signals in the optical domain [38, 39, 112]. Similar to microwave frequency mulitiplication, the use of MZM is also considered to be a competitive approach to generating binary digital modulation signals. Microwave PSK and FSK signals have been proposed and realized based on commercial MZMs [38, 39, 112]. However, microwave ASK signal as a fundamental digital modulation format in wireless communication has rarely been realized using MZM. In this section, we introduce our recent work on microwave signal multiplication and ASK modulation based on an integrated silicon modulator.

We first propose a simple scheme to obtain frequency-multiplicated microwave signals [113]. **Figure 23** illustrates the schematic illustration of the proposed photonic frequency-multiplicated microwave signal generation system using an integrated silicon MZM. CW light from a tunable laser diode (TLD) is sent to the MZM. The driving signal and the DC-bias are combined by a bias-tee and applied to the MZM. The output light intensity of the MZM can be written as:

$$\begin{aligned} I \;=\; & \tfrac{1}{2} I_0 \left[1 + J_0(m) \cos \varphi_0 \right] + I_0 \cos \varphi_0 \sum_{n=1}^{\infty} (-1)^n J_{2n}(m) \cos(2n\, \omega_{\mathrm{RF}}\, t) \\ & + I_0 \sin \varphi_0 \sum_{n=1}^{\infty} (-1)^n J_{2n-1}(m) \cos \left[(2n-1)\, \omega_{RF}\, t \right] \end{aligned} \tag{1}$$

where $m = \pi V_{RF}/V_{\pi}$ is the modulation indice of the MZM. I_0 is the intensity of the input optical carrier. $\phi_0 = \pi V_b/V_{\pi}$ is the constant phase difference between the two arms determined by the constant DC-bias voltage V_b. V_{π} is the half-wave voltage of the MZM. V_{RF} and ω_{RF} are the amplitude and angular frequency of the applied electrical drive voltage, respectively. It can be seen from Eq. (1) that if the modulator is biased at V_{π}, the odd components will be suppressed. Ignoring the high-order harmonic wave, a frequency-doubled microwave signal is obtained. In addition, by adjusting the driving microwave signal amplitude to let $J_2(m) = 0$, the quadruple response will dominate the output, and a frequency-quadrupled signal can be obtained. Similarly, a frequency-tripled signal is generated by suppressing the even components and $J_1(m)$ term of the signal.

We investigate the generation of frequency-doubled microwave signal. **Figure 24(a)** and **(b)** shows the wave-forms of the original 500-MHz driving signal and the generated 1-GHz signal. **Figure 24(c)** and **(d)** shows the obtained 2-GHz signal when the driving signal frequency is 1 GHz.

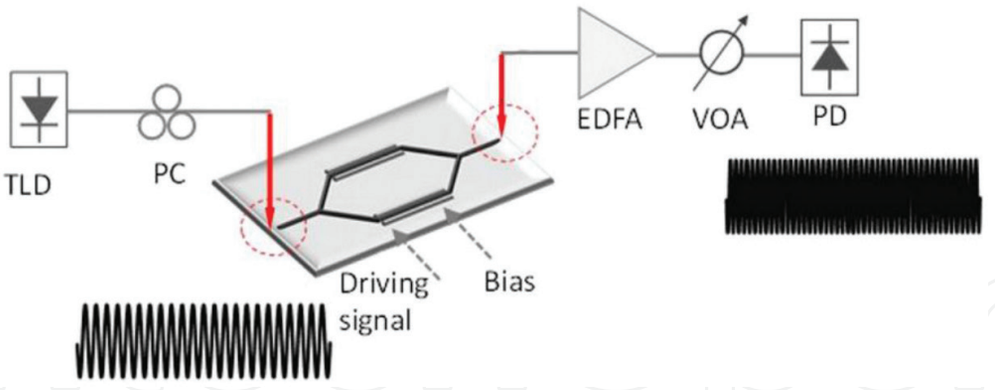


Figure 23. Schematic illustration of the proposed photonic-assisted microwave signal multiplication.

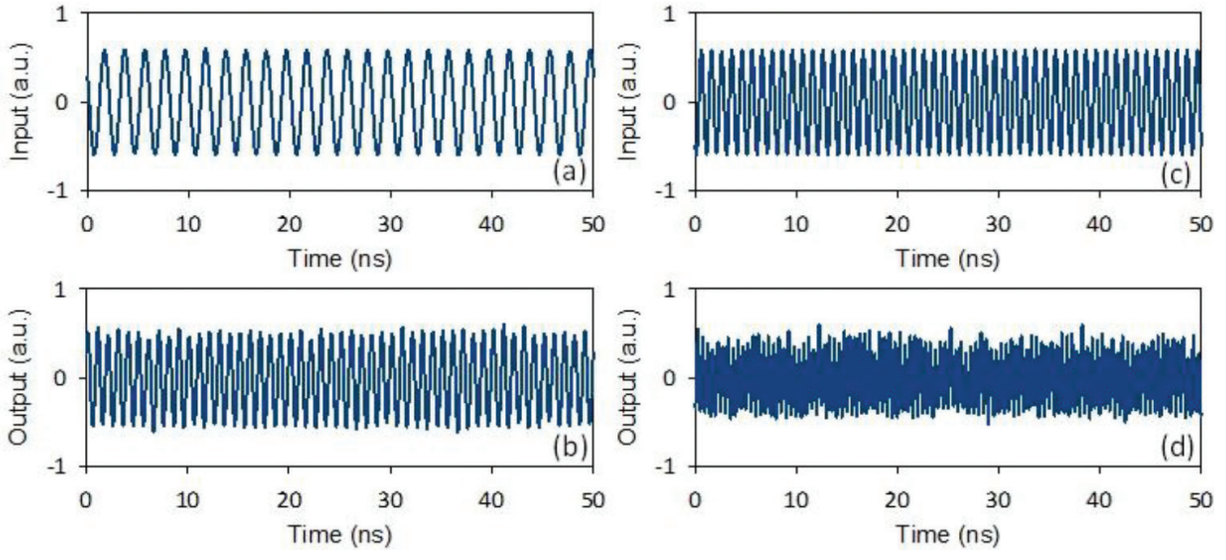


Figure 24. Waveforms of (a) the input 500-MHz driving signal, (b) the generated 1-GHz frequency-doubled signal, (c) the input 1-GHz driving signal, and (d) the generated 2-GHz frequency-doubled signal.

Using the fabricated integrated MZM, we also demonstrate the feasibility of microwave ASK modulation using an integrated photonic approach [113]. **Figure 25** illustrates the schematic illustration of the proposed photonic microwave ASK signal modulation system using an integrated silicon MZM. The microwave carrier signal and the binary coding signal s(t) are applied to the two RF ports of the MZM, respectively. The AC term of the detected signal at the output of the PD can be written as:

$$i_{AC} \propto 2J_1(m)\cos(\omega_{RF}t)\sin(\gamma s(t)-\varphi_0)+J_0(m)\cos(\gamma s(t)-\varphi_0) \quad (2)$$

where ω_{RF}, m, $V_{RF,}$ V_π, and ϕ_0 are defined as previously mentioned. $\gamma=\pi V_s/V_\pi$ is the modulation index in the arm where the binary coding signal is applied. Assuming $\phi_0 = 0$, Eq. (2) can be simplified as:

http://dx.doi.org/10.5772/66322

$$i_{AC} \propto 2J_1(m)\cos(\omega_{RF}t)\sin(\gamma s(t))+J_0(m)\cos(\gamma s(t)) \tag{3}$$

The second term in Eq. (3) is located in the baseband, which can be easily eliminated by an electric filter. Assuming $\gamma = \pi/2$, the amplitude of the obtained signal is:

$$i = \begin{cases} 2J_1(m)\cos(\omega_{RF}t) & s(t)=1 \\ 0 & s(t)=0 \end{cases} \tag{4}$$

As can be seen, the amplitude of the carrier is "1" with bit "1", and "0" with bit "0". Therefore, two-level microwave ASK signal is generated.

Figure 26(a) shows the waveforms of the original 50-Mb/s baseband signal with a pattern of "110100101101001011". The original 1-GHz microwave carrier is shown in **Figure 26(b)**. **Figure 26(c)** shows the modulated microwave ASK signal.

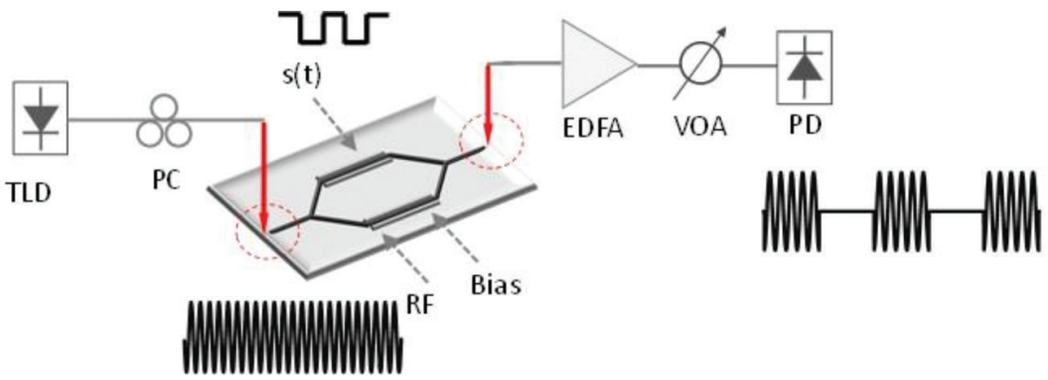


Figure 25. Schematic illustration of the proposed photonic microwave ASK signal generator.

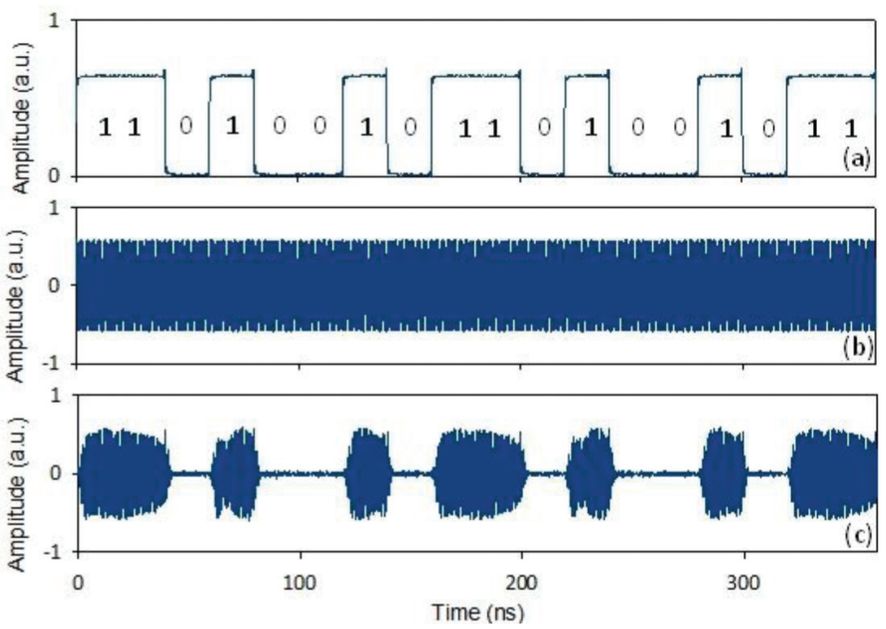


Figure 26. Waveforms of (a) the original 50-Mb/s baseband signal with a pattern of "110100101101001011", (b) original 1-GHz microwave carrier signal, and (c) the output microwave ASK signal.

5. Discussion

In summary, we review our recent works in chip-scale microwave photonic signal processing, including on-chip analog links, MWP filters, and photonic generation of microwave. As a new research topic, integrated MWP has just started to bloom and is set to have a bright future. After evaluating linearity performance of the on-chip analog links, future works may focus on increasing the linearities or decreasing nonlinearities of the on-chip analog links. As to MWP filters, more high performance silicon MWP filters will be demonstrated, involving resonators, photonic crystals, or other silicon photonic devices. In addition, more nonlinear optics can be used for MWP filters. For example, four-wave mixing (FWM) for MWP filtering has been realized [114, 115]. The demonstrated microwave signal multiplication and ASK modulation are still operated in low-frequency region. By optimizing the device design, the operation frequency can be improved and the power consumption can be further reduced. In addition to on-chip analog links, MWP filters, and photonic generation of microwave, silicon photonics can be also adopted to accelerate the success of versatile MWP signal processing functionalities, including arbitrary waveform generation, on-chip pulse shaping, delay line, beamformer, and more.

6. Conclusion

In this chapter, we have reviewed recent research efforts toward on-chip microwave photonic signal processing.

1. Using the fabricated silicon photonic devices, we evaluate the performance of on-chip analog signal transmission. The degradations level of SHD and THD are evaluated.
2. Various types of MWP filters are introduced, and the impact of optical nonlinearities to MWP filters is also discussed.
3. Photonic-assisted microwave signal multiplication/modulation: we propose a simple scheme to obtain frequency-multiplicated microwave signals or amplitude-coded microwave signals based on a single integrated silicon MZM. A 2-GHz frequency-doubled microwave signal is generated using a 1-GHz driving signal. A 50-Mb/s binary amplitude-coded 1-GHz microwave signal is also successfully generated in the experiment.

With future improvement, one would also expect to see more photonic-assisted microwave signal processing applications exploiting compact-integrated silicon photonic devices.

Acknowledgements

This work was supported by the National Program for Support of Top-Notch Young Professionals, the National Natural Science Foundation of China (NSFC) under grants 11574001, 11274131, and 61222502, the Program for New Century Excellent Talents in University under grant NCET-11-0182, the National Basic Research Program of China

(973 Program) under grant 2014CB340004, the Wuhan Science and Technology Plan Project under grant 2014070404010201, the Fundamental Research Funds for the Central Universities (HUST) under grants 2012YQ008 and 2013ZZGH003. The authors thank the Center of Micro-Fabrication and Characterization (CMFC) of WNLO for the support in the manufacturing process of silicon waveguides. The authors also thank to the facility support of the Center for Nanoscale Characterization and Devices of WNLO.

Author details

Jian Wang* and Yun Long

*Address all correspondence to: jwang@hust.edu.cn

Wuhan National Laboratory for Optoelectronics, School of Optical and Electronic Information, Huazhong University of Science and Technology, Wuhan, Hubei, China

References

[1] R. Soref, "The past, present, and future of silicon photonics," IEEE J. Sel. Top. Quantum Electron. 12, 1678–1687 (2006).

[2] B. Jalali, and S. Fathpour, "Silicon photonics," J. Lightwave Technol. 24, 4600–4615 (2006).

[3] M. Hochberg, and T. Baehr-Jones, "Towards fabless silicon photonics," Nat. Photonics. 4, 492–494 (2010).

[4] M. Asghari, and A. V. Krishnamoorthy, "Silicon photonics: Energy-efficient communication," Nat. Photonics. 5, 268–270 (2011).

[5] M. Soljačić, M. Ibanescu, S. G. Johnson, Y. Fink, and J. Joannopoulos, "Optimal bistable switching in nonlinear photonic crystals," Phys. Rev. E. 66, 055601 (2002).

[6] Y. Akahane, T. Asano, B.-S. Song, and S. Noda, "Fine-tuned high-Q photonic-crystal nanocavity," Opt. Express. 13, 1202–1214 (2005).

[7] P. Barclay, K. Srinivasan, and O. Painter, "Nonlinear response of silicon photonic crystal microresonators excited via an integrated waveguide and fiber taper," Opt. Express. 13, 801–820 (2005).

[8] M. Notomi, A. Shinya, S. Mitsugi, G. Kira, E. Kuramochi, and T. Tanabe, "Optical bistable switching action of Si high-Q photonic-crystal nanocavities," Opt. Express. 13, 2678–2687 (2005).

[9] Y. Zhang, D. Li, C. Zeng, Y. Shi, Z. Huang, J. Yu, and J. Xia, "Ultralow power nonlinear response in an Si photonic crystal nanocavity," IEEE Photon. J. 5, 6601409 (2013).

[10] Y. Zhang, D. Li, C. Zeng, Z. Huang, Y. Wang, Q. Huang, Y. Wu, J. Yu, and J. Xia, "Silicon optical diode based on cascaded photonic crystal cavities," Opt. Lett. 39, 1370–1373 (2014).

[11] W. Bogaerts, R. Baets, P. Dumon, V. Wiaux, S. Beckx, D. Taillaert, B. Luyssaert, J. Van Campenhout, P. Bienstman, and D. Van Thourhout, "Nanophotonic waveguides in silicon-on-insulator fabricated with CMOS technology," J. Lightwave Technol. 23, 401–412 (2005).

[12] B. E. Little, S. T. Chu, H. A. Haus, J. Foresi, and J. P. Laine, "Microring resonator channel dropping filters," J. Lightwave Technol. 15, 998–1005 (1997).

[13] B. E. Little, J. Foresi, G. Steinmeyer, E. Thoen, S. Chu, H. Haus, E. Ippen, L. Kimerling, and W. Greene, "Ultra-compact Si-SiO 2 microring resonator optical channel dropping filters," IEEE Photon. Technol. Lett. 10, 549–551 (1998).

[14] B. Little, S. Chu, W. Pan, and Y. Kokubun, "Microring resonator arrays for VLSI photonics," IEEE Photon. Technol. Lett. 12, 323–325 (2000).

[15] G. Priem, P. Dumon, W. Bogaerts, D. Van Thourhout, G. Morthier, and R. Baets, "Optical bistability and pulsating behaviour in Silicon-On-Insulator ring resonator structures," Opt. Express. 13, 9623–9628 (2005).

[16] W. Bogaerts, P. De Heyn, T. Van Vaerenbergh, K. De Vos, S. Kumar Selvaraja, T. Claes, P. Dumon, P. Bienstman, D. Van Thourhout, and R. Baets, "Silicon microring resonators," Laser & Photonics Rev. 6, 47–73 (2012).

[17] T. Barwicz, H. Byun, F. Gan, C. Holzwarth, M. Popovic, P. Rakich, M. Watts, E. Ippen, F. Kärtner, and H. Smith, "Silicon photonics for compact, energy-efficient interconnects [Invited]," J. Opt. Netw. 6, 63–73 (2007).

[18] J. S. Levy, A. Gondarenko, M. A. Foster, A. C. Turner-Foster, A. L. Gaeta, and M. Lipson, "CMOS-compatible multiple-wavelength oscillator for on-chip optical interconnects," Nat. Photonics. 4, 37–40 (2010).

[19] X. Xiao, H. Xu, X. Li, Z. Li, Y. Yu, and J. Yu, "High-speed on-chip photonic link based on ultralow-power microring modulator," in *Optical Fiber Communication Conference* (Optical Society of America, 2014), paper Tu2E. 6.

[20] J. K. Doylend, and A. P. Knights, "The evolution of silicon photonics as an enabling technology for optical interconnection," Laser & Photonics Rev. 6, 504–525 (2012).

[21] Y. Vlasov, "Silicon photonics for next generation computing systems," in *European Conference on Optical Communications*(2008), paper 1–2.

[22] L. Chen, K. Preston, S. Manipatruni, and M. Lipson, "Integrated GHz silicon photonic interconnect with micrometer-scale modulators and detectors," Opt. Express. 17, 15248–15256 (2009).

[23] C. Sun, M. T. Wade, Y. Lee, J. S. Orcutt, L. Alloatti, M. S. Georgas, A. S. Waterman, J. M. Shainline, R. R. Avizienis, and S. Lin, "Single-chip microprocessor that communicates directly using light," Nature. 528, 534–538 (2015).

[24] C. Sun, M. Georgas, J. Orcutt, B. Moss, Y.-H. Chen, J. Shainline, M. Wade, K. Mehta, K. Nammari, and E. Timurdogan, "A monolithically-integrated chip-to-chip optical link in bulk CMOS," IEEE J. Solid-St. Circ. 50, 828–844 (2015).

[25] Q. Li, Y. Liu, K. Padmaraju, R. Ding, D. F. Logan, J. J. Ackert, A. P. Knights, T. Baehr-Jones, M. Hochberg, and K. Bergman, "10-Gb/s BPSK link using silicon microring resonators for modulation and demodulation," in *Optical Fiber Communication Conference* (Optical Society of America, 2014), paper Tu2E. 5.

[26] D. Marris-Morini, L. Virot, C. Baudot, J.-M. Fédéli, G. Rasigade, D. Perez-Galacho, J.-M. Hartmann, S. Olivier, P. Brindel, and P. Crozat, "A 40 Gbit/s optical link on a 300-mm silicon platform," Opt. Express. 22, 6674–6679 (2014).

[27] A. Narasimha, B. Analui, Y. Liang, T. J. Sleboda, S. Abdalla, E. Balmater, S. Gloeckner, D. Guckenberger, M. Harrison, and R. G. Koumans, "A fully integrated 4× 10-Gb/s DWDM optoelectronic transceiver implemented in a standard 0.13 μm CMOS SOI technology," IEEE J. Solid-St. Circ. 42, 2736–2744 (2007).

[28] C. Doerr, L. Chen, L. Buhl, and Y.-K. Chen, "Eight-Channel SiO/Si N/Si/Ge CWDM Receiver," IEEE Photon. Technol. Lett. 23, 1201–1203 (2011).

[29] C. Doerr, and T. Taunay, "Silicon photonics core-, wavelength-, and polarization-diversity receiver," IEEE Photon. Technol. Lett. 9, 597–599 (2011).

[30] C. R. Doerr, N. K. Fontaine, and L. L. Buhl, "PDM-DQPSK silicon receiver with integrated monitor and minimum number of controls," IEEE Photon. Technol. Lett. 24, 697–699 (2012).

[31] J. Klamkin, F. Gambini, S. Faralli, A. Malacarne, G. Meloni, G. Berrettini, G. Contestabile, and L. Potì, "A 100-Gb/s noncoherent silicon receiver for PDM-DBPSK/DQPSK signals," Opt. Express. 22, 2150–2158 (2014).

[32] P. Dong, C. Xie, L. Chen, L. L. Buhl, and Y.-K. Chen, "112-Gb/s monolithic PDM-QPSK modulator in silicon," Opt. Express. 20, B624-B629 (2012).

[33] A. Shastri, M. Webster, G. Jeans, P. Metz, S. Sunder, B. Chattin, B. Dama, and K. Shastri, "Experimental demonstration of ultra-low-power single polarization 56 Gb/s QAM-16 generation without DAC using CMOS photonics," in *2014 The European Conference on Optical Communication (ECOC)* (2014).

[34] C. R. Doerr, L. Chen, D. Vermeulen, T. Nielsen, S. Azemati, S. Stulz, G. McBrien, X.-M. Xu, B. Mikkelsen, and M. Givehchi, "Single-chip silicon photonics 100-Gb/s coherent transceiver," in *Optical Fiber Communication Conference* (Optical Society of America, 2014), paper Th5C. 1.

[35] J. Yao, "Microwave photonics," J. Lightwave Technol. 27, 314–335 (2009).

[36] J. Capmany, J. Mora, I. Gasulla, J. Sancho, J. Lloret, and S. Sales, "Microwave photonic signal processing," J. Lightwave Technol. 31, 571–586 (2013).

[37] F. Liu, T. Wang, Z. Zhang, M. Qiu, and Y. Su, "On-chip photonic generation of ultra-wideband monocycle pulses," Electron. Lett. 45, 1 (2009).

[38] P. Cao, X. Hu, L. Zhang, J. Wu, X. Jiang, and Y. Su, "Photonic generation of microwave frequency shift keying signal using a single-drive Mach–Zehnder modulator," Opt. Express. 22, 14433–14440 (2014).

[39] Z. Tang, T. Zhang, F. Zhang, and S. Pan, "Photonic generation of a phase-coded microwave signal based on a single dual-drive Mach–Zehnder modulator," Opt. Lett. 38, 5365–5368 (2013).

[40] P. Xiang, X. Zheng, H. Zhang, Y. Li, and Y. Chen, "A novel approach to photonic generation of RF binary digital modulation signals," Opt. Express. 21, 631–639 (2013).

[41] D. Zhang, X. Feng, X. Li, K. Cui, F. Liu, and Y. Huang, "Tunable and reconfigurable bandstop microwave photonic filter based on integrated microrings and Mach–Zehnder interferometer," J. Lightwave Technol. 31, 3668–3675 (2013).

[42] Y. Long, and J. Wang, "All-optical tuning of a nonlinear silicon microring assisted microwave photonic filter: theory and experiment," Opt. Express. 23, 17758–17771 (2015).

[43] Y. Long, and J. Wang, "Ultra-high peak rejection notch microwave photonic filter using a single silicon microring resonator," Opt. Express 23, 17739–17750 (2015).

[44] D. Marpaung, B. Morrison, M. Pagani, R. Pant, D.-Y. Choi, B. Luther-Davies, S. J. Madden, and B. J. Eggleton, "Low-power, chip-based stimulated Brillouin scattering microwave photonic filter with ultrahigh selectivity," Optica. 2, 76–83 (2015).

[45] N. Ehteshami, W. Zhang, and J. Yao, "Optically tunable full 360° microwave photonic phase shifter using three cascaded silicon-on-insulator microring resonators," Opt. Commun. 373, 53–58 (2016).

[46] J. Wu, J. Peng, B. Liu, T. Pan, H. Zhou, J. Mao, Y. Yang, C. Qiu, and Y. Su, "Passive silicon photonic devices for microwave photonic signal processing," Opt. Commun. 373, 44–52 (2016).

[47] A. Casas-Bedoya, B. Morrison, M. Pagani, D. Marpaung, and B. J. Eggleton, "Tunable narrowband microwave photonic filter created by stimulated Brillouin scattering from a silicon nanowire," Opt. Lett. 40, 4154–4157 (2015).

[48] A. Zheng, J. Dong, L. Zhou, X. Xiao, Q. Yang, X. Zhang, and J. Chen, "Fractional-order photonic differentiator using an on-chip microring resonator," Opt. Lett. 39, 6355–6358 (2014).

[49] S. Yan, Y. Zhang, J. Dong, A. Zheng, S. Liao, H. Zhou, Z. Wu, J. Xia, and X. Zhang, "Operation bandwidth optimization of photonic differentiators," Opt. Express. 23, 18925–18936 (2015).

[50] Y. Yu, F. Jiang, H. Tang, L. Xu, X. Liu, J. Dong, and X. Zhang, "Reconfigurable photonic temporal differentiator based on a dual-drive Mach-Zehnder modulator," Opt. Express. 24, 11739–11748 (2016).

[51] H. Jiang, D. Marpaung, M. Pagani, K. Vu, D.-Y. Choi, S. J. Madden, L. Yan, and B. J. Eggleton, "Wide-range, high-precision multiple microwave frequency measurement using a chip-based photonic Brillouin filter," Optica. 3, 30–34 (2016).

[52] M. Pagani, B. Morrison, Y. Zhang, A. Casas-Bedoya, T. Aalto, M. Harjanne, M. Kapulainen, B. J. Eggleton, and D. Marpaung, "Low-error and broadband microwave frequency measurement in a silicon chip," Optica. 2, 751–756 (2015).

[53] J. Du, and J. Wang, "Experimental performance evaluation of analog signal transmission in a silicon microring resonator," Opt. Lett. 40, 1181–1184 (2015).

[54] C. Gui, Y. Zhang, J. Du, J. Xia, and J. Wang, "Experimental demonstration of analog signal transmission in a silicon photonic crystal L3 resonator," Opt. Express. 23, 13916–13923 (2015).

[55] W. Liu, M. Li, R. S. Guzzon, E. J. Norberg, J. S. Parker, L. A. Coldren, and J. Yao, "A photonic temporal integrator with an ultra-long integration time window based on an InP-InGaAsP integrated ring resonator," J. Lightwave Technol. 32, 3654–3659 (2014).

[56] J. Zhang, and J. Yao, "Microwave photonic integrator based on a multichannel fiber Bragg grating," Opt. Lett. 41, 273–276 (2016).

[57] H. P. Bazargani, M. Burla, and J. Azaña, "Experimental demonstration of sub-picosecond optical pulse shaping in silicon based on discrete space-to-time mapping," Opt. Lett. 40, 5423–5426 (2015).

[58] H. P. Bazargani, and J. Azaña, "Optical pulse shaping based on discrete space-to-time mapping in cascaded co-directional couplers," Opt. Express. 23, 23450–23461 (2015).

[59] T. Yang, J. Dong, L. Liu, S. Liao, S. Tan, L. Shi, D. Gao, and X. Zhang, "Experimental observation of optical differentiation and optical Hilbert transformation using a single SOI microdisk chip," Sci. Rep. 4, 3960 (2014).

[60] J. Wang, H. Shen, L. Fan, R. Wu, B. Niu, L. T. Varghese, Y. Xuan, D. E. Leaird, X. Wang, and F. Gan, "Reconfigurable radio-frequency arbitrary waveforms synthesized in a silicon photonic chip," Nat. Commun. 6, 5957 (2015).

[61] M. H. Khan, H. Shen, Y. Xuan, L. Zhao, S. Xiao, D. E. Leaird, A. M. Weiner, and M. Qi, "Ultrabroad-bandwidth arbitrary radiofrequency waveform generation with a silicon photonic chip-based spectral shaper," Nat. Photonics. 4, 117–122 (2010).

[62] J. McKinney, D. Leaird, and A. Weiner, "Millimeter-wave arbitrary waveform generation with a direct space-to-time pulse shaper," Opt. Lett. 27, 1345–1347 (2002).

[63] S. Liao, Y. Ding, J. Dong, T. Yang, X. Chen, D. Gao, and X. Zhang, "Arbitrary waveform generator and differentiator employing an integrated optical pulse shaper," Opt. Express. 23, 12161–12173 (2015).

[64] J. O'reilly, P. Lane, R. Heidemann, and R. Hofstetter, "Optical generation of very narrow linewidth millimetre wave signals," Electron. Lett. 28, 2309–2311 (1992).

[65] G. Qi, J. Yao, J. Seregelyi, S. Paquet, and C. Bélisle, "Generation and distribution of a wide-band continuously tunable millimeter-wave signal with an optical external modulation technique," IEEE Trans. Microwave Theory Tech. 53, 3090–3097 (2005).

[66] M. Burla, C. G. Roeloffzen, L. Zhuang, D. Marpaung, M. R. Khan, P. Maat, K. Dijkstra, A. Leinse, M. Hoekman, and R. Heideman, "System integration and radiation pattern measurements of a phased array antenna employing an integrated photonic beamformer for radio astronomy applications," Appl. Optics. 51, 789–802 (2012).

[67] H. Zmuda, R. A. Soref, P. Payson, S. Johns, and E. N. Toughlian, "Photonic beamformer for phased array antennas using a fiber grating prism," IEEE Photon. Technol. Lett. 9, 241–243 (1997).

[68] N.-N. Feng, P. Dong, D. Feng, W. Qian, H. Liang, D. C. Lee, J. B. Luff, A. Agarwal, T. Banwell, and R. Menendez, "Thermally-efficient reconfigurable narrowband RF-photonic filter," Opt. Express. 18, 24648–24653 (2010).

[69] Y. Yue, H. Huang, L. Zhang, J. Wang, J.-Y. Yang, O. F. Yilmaz, J. S. Levy, M. Lipson, and A. E. Willner, "UWB monocycle pulse generation using two-photon absorption in a silicon waveguide," Opt. Lett. 37, 551–553 (2012).

[70] X. Wang, W. Shi, H. Yun, S. Grist, N. A. Jaeger, and L. Chrostowski, "Narrow-band waveguide Bragg gratings on SOI wafers with CMOS-compatible fabrication process," Opt. Express. 20, 15547–15558 (2012).

[71] M. L. Farwell, W. S. Chang, and D. R. Huber, "Increased linear dynamic range by low biasing the Mach-Zehnder modulator," IEEE Photon. Technol. Lett. 5, 779–782 (1993).

[72] A. Khilo, C. M. Sorace, and F. X. Kärtner, "Broadband linearized silicon modulator," Opt. Express. 19, 4485–4500 (2011).

[73] M. Streshinsky, A. Ayazi, Z. Xuan, A. E.-J. Lim, G.-Q. Lo, T. Baehr-Jones, and M. Hochberg, "Highly linear silicon traveling wave Mach-Zehnder carrier depletion modulator based on differential drive," Opt. Express. 21, 3818–3825 (2013).

[74] J. Cardenas, P. A. Morton, J. B. Khurgin, A. Griffith, C. B. Poitras, K. Preston, and M. Lipson, "Linearized silicon modulator based on a ring assisted Mach Zehnder inteferometer," Opt. Express. 21, 22549–22557 (2013).

[75] M. LaGasse, W. Charczenko, M. Hamilton, and S. Thaniyavarn, "Optical carrier filtering for high dynamic range fibre optic links," Electron. Lett. 30, 2157–2158 (1994).

[76] P. Li, L. Yan, T. Zhou, W. Li, Z. Chen, W. Pan, and B. Luo, "Improvement of linearity in phase-modulated analog photonic link," Opt. Lett. 38, 2391–2393 (2013).

[77] H. Huang, Y. Yue, L. Zhang, C. Chase, D. Parekh, F. Sedgwick, M. Wu, C. Chang-Hasnain, M. Tur, and A. Willner, "Analog signal transmission in a high-contrast-gratings-based hollow-core-waveguide," J. Lightwave Technol. 30, 3640–3646 (2012).

[78] M. Song, L. Zhang, R. G. Beausoleil, and A. E. Willner, "Nonlinear distortion in a silicon microring-based electro-optic modulator for analog optical links," IEEE J. Sel. Top. Quantum Electron. 16, 185–191 (2010).

[79] A. Ayazi, T. Baehr-Jones, Y. Liu, A. E.-J. Lim, and M. Hochberg, "Linearity of silicon ring modulators for analog optical links," Opt. Express. 20, 13115–13122 (2012).

[80] S. J. Spector, S. Yegnanarayanan, R. Swint, T. M. Lyszczarz, and P. W. Juodawlkis, "Two-tone measurement of the nonlinear behavior of a silicon-on-insulator (SOI) ring resonator," in *CLEO: Applications and Technology* (Optical Society of America, 2012), paper JW4A. 74.

[81] X. Luo, X. Tu, J. Song, L. Ding, Q. Fang, T.-Y. Liow, M. Yu, and G.-Q. Lo, "Slope efficiency and spurious-free dynamic range of silicon Mach-Zehnder modulator upon carrier depletion and injection effects," Opt. Express. 21, 16570–16577 (2013).

[82] D. Marpaung, C. Roeloffzen, R. Heideman, A. Leinse, S. Sales, and J. Capmany, "Integrated microwave photonics," Laser & Photonics Rev. 7, 506–538 (2013).

[83] R. A. Minasian, "Photonic signal processing of microwave signals," IEEE Trans. Microwave Theory Tech. 54, 832–846 (2006).

[84] J. Capmany, B. Ortega, D. Pastor, and S. Sales, "Discrete-time optical processing of microwave signals," J. Lightwave Technol. 23, 702 (2005).

[85] J. Capmany, B. Ortega, and D. Pastor, "A tutorial on microwave photonic filters," J. Lightwave Technol. 24, 201–229 (2006).

[86] J. Mora, B. Ortega, A. Díez, J. L. Cruz, M. V. Andrés, J. Capmany, and D. Pastor, "Photonic microwave tunable single-bandpass filter based on a Mach-Zehnder interferometer," J. Lightwave Technol. 24, 2500–2509 (2006).

[87] B. Vidal, M. Piqueras, and J. Marti, "Tunable and reconfigurable photonic microwave filter based on stimulated Brillouin scattering," Opt. Lett. 32, 23–25 (2007).

[88] W. Zhang, and R. A. Minasian, "Widely tunable single-passband microwave photonic filter based on stimulated Brillouin scattering," IEEE Photon. Technol. Lett. 23, 1775–1777 (2011).

[89] L. Gao, X. Chen, and J. Yao, "Tunable microwave photonic filter with a narrow and flat-top passband," IEEE Microw. Wireless Compon. Lett. 23, 362–364 (2013).

[90] W. Li, and J. Yao, "A narrow-passband frequency-tunable microwave photonic filter with an improved dynamic range," in *Optical Fiber Communication Conference* (Optical Society of America, Anaheim, California, 2013), paper OTu2H. 3.

[91] P. K. Yu, "A novel digitally tunable microwave-photonic notch filter using differential group-delay module," IEEE Photon. Technol. Lett. 15 (2003).

[92] P. Alipour, A. A. Eftekhar, A. H. Atabaki, Q. Li, S. Yegnanarayanan, C. K. Madsen, and A. Adibi, "Fully reconfigurable compact RF photonic filters using high-Q silicon microdisk resonators," Opt. Express. 19, 15899–15907 (2011).

[93] D. Zhang, X. Feng, and Y. Huang, "Tunable and reconfigurable bandpass microwave photonic filters utilizing integrated optical processor on silicon-on-insulator substrate," IEEE Photon. Technol. Lett. 24, 1502–1505 (2012).

[94] J. Dong, L. Liu, D. Gao, Y. Yu, A. Zheng, T. Yang, and X. Zhang, "Compact notch microwave photonic filters using on-chip integrated microring resonators," IEEE Photon. J. 5, 5500307–5500307 (2013).

[95] M. S. Rasras, K.-Y. Tu, D. M. Gill, Y.-K. Chen, A. E. White, S. S. Patel, A. Pomerene, D. Carothers, J. Beattie, and M. Beals, "Demonstration of a tunable microwave-photonic

notch filter using low-loss silicon ring resonators," J. Lightwave Technol. 27, 2105–2110 (2009).

[96] J. Palací, G. E. Villanueva, J. V. Galán, J. Marti, and B. Vidal, "Single bandpass photonic microwave filter based on a notch ring resonator," IEEE Photon. Technol. Lett. 22, 1276–1278 (2010).

[97] D. Zhang, X. Feng, and Y. Huang, "Reconfigurable microwave photonic filter based on parallel-cascaded microrings assisted with a Mach–Zehnder interferometer," J. Opt. 14, 065502 (2012).

[98] D. Marpaung, B. Morrison, R. Pant, C. Roeloffzen, A. Leinse, M. Hoekman, R. Heideman, and B. J. Eggleton, "Si_3N_4 ring resonator-based microwave photonic notch filter with an ultrahigh peak rejection," Opt. Express 21, 23286–23294 (2013).

[99] D. Marpaung, B. Morrison, R. Pant, C. Roeloffzen, A. Leinse, M. Hoekman, R. Heideman, and B. J. Eggleton, "Ultrahigh suppression and reconfigurable RF photonic notch filter using a silicon nitride ring resonator," in *2014 Conference on Lasers and Electro-Optics (CLEO)*, (2014), paper 1–2.

[100] L. Goldberg, H. Taylor, J. Weller, and D. Bloom, "Microwave signal generation with injection-locked laser diodes," Electron. Lett. 19, 491–493 (1983).

[101] R. Ramos, and A. Seeds, "Fast heterodyne optical phase-lock loop using double quantum well laser diodes," Electron. Lett. 28, 82–83 (1992).

[102] J. O'Reilly, and P. Lane, "Remote delivery of video services using mm-waves and optics," J. Lightwave Technol. 12, 369–375 (1994).

[103] G. Qi, J. Yao, J. Seregelyi, S. Paquet, and C. Bélisle, "Optical generation and distribution of continuously tunable millimeter-wave signals using an optical phase modulator," J. Lightwave Technol. 23, 2687–2695 (2005).

[104] J. Yu, Z. Jia, L. Yi, Y. Su, G.-K. Chang, and T. Wang, "Optical millimeter-wave generation or up-conversion using external modulators," IEEE Photon. Technol. Lett. 18, 265–267 (2006).

[105] W. Li, and J. Yao, "Investigation of photonically assisted microwave frequency multiplication based on external modulation," IEEE Trans. Microwave Theory Tech. 58, 3259–3268 (2010).

[106] L. Gao, W. Liu, X. Chen, and J. Yao, "Photonic-assisted microwave frequency multiplication with a tunable multiplication factor," Opt. Lett. 38, 4487–4490 (2013).

[107] B. Chen, S. Zheng, H. Chi, X. Zhang, and X. Jin, "An optical millimeter-wave generation technique based on phase modulation and Brillouin-assisted notch-filtering," IEEE Photon. Technol. Lett. 20, 2057–2059 (2008).

[108] A. Wiberg, P. Pérez-Millán, M. V. Andrés, and P. O. Hedekvist, "Microwave-photonic frequency multiplication utilizing optical four-wave mixing and fiber Bragg gratings," J. Lightwave Technol. 24, 329 (2006).

[109] C. Zhang, L. Wang, and K. Qiu, "Proposal for all-optical generation of multiple-frequency millimeter-wave signals for RoF system with multiple base stations using FWM in SOA," Opt. Express. 19, 13957–13962 (2011).

[110] B. Vidal, "Photonic millimeter-wave frequency multiplication based on cascaded four-wave mixing and polarization pulling," Opt. Lett. 37, 5055–5057 (2012).

[111] J. Zheng, H. Wang, W. Li, L. Wang, T. Su, J. Liu, and N. Zhu, "Photonic-assisted microwave frequency multiplier based on nonlinear polarization rotation," Opt. Lett. 39, 1366–1369 (2014).

[112] J. Chou, H. Yan, and B. Jalali, "Adaptive RF-photonic arbitrary waveform generator," IEEE Photon. Technol. Lett. 15, 581–583 (2003).

[113] Y. Long, L. Zhou, and J. Wang, "Photonic-assisted microwave signal multiplication and modulation using a silicon Mach–Zehnder modulator," Sci. Rep. 6, 20215 (2016).

[114] V. R. Supradeepa, C. M. Long, R. Wu, F. Ferdous, E. Hamidi, D. E. Leaird, and A. M. Weiner, "Comb-based radiofrequency photonic filters with rapid tunability and high selectivity," Nat. Photonics 6, 186–194 (2012).

[115] B. Vidal Rodriguez, J. Palací López, and J. Capmany Francoy, "Reconfigurable photonic microwave filter based on four-wave mixing," in *IEEE Photonics Journal* (Institute of Electrical and Electronics Engineers (IEEE), 2012), paper 759–764.

IntechOpen

IntechOpen

IntechOpen